ER-anchored protein sorting controls the fate of two proteasome activators for intracellular organelle communication during proteotoxic stress

Gautier Langin[1,2], Margot Raffeiner[1], David Biermann[2], Mirita Franz-Wachtel[3], Daniela Spinti[4], Frederik Börnke[4,5], Boris Macek[3], Suayib Üstün[1,*]

[1] Faculty of Biology & Biotechnology, Ruhr-University Bochum, Bochum, Germany
[2] Center for Plant Molecular Biology (ZMBP), University of Tübingen, Tübingen, Germany
[3] Institute for Cell Biology, Department of Quantitative Proteomics, University of Tübingen, Tübingen, Germany Method section for MS/MS analysis
[4] Leibniz-Institute of Vegetable and Ornamental Crops (IGZ), Großbeeren, Germany
[5] Institute of Biochemistry and Biology, University of Potsdam, Potsdam, Germany

[*]Correspondence: suayb.uestuen@rub.de

Summary

Proteotoxic stress, characterized by the accumulation of damaged proteins, poses a significant challenge to cellular homeostasis. To mitigate proteotoxicity eukaryotes employ the proteasome that is regulated by proteasome activators, e.g. transcription factors that promote gene expression of proteasome subunits. As proteotoxicity originates in different compartments, cells need to perceive signals from various locations. Understanding which components integrate signals to address proteotoxicity is essential to develop strategies to cope with proteotoxicity but remain elusive. Here, we identify that the proteasome autoregulatory feedback loop acts as a gatekeeper to facilitate the communication between nucleus and chloroplast. We reveal that the ER-anchored protein sorting system (ERAPS) controls the proteasomal degradation or nuclear translocation of proteasome activators NAC53 and NAC78. While both transcription factors activate the proteasome gene expression, they repress photosynthesis-associated nuclear genes during proteotoxicity. Collectively, our discoveries provide a novel conceptual framework in which the proteasome autoregulatory feedback loop coordinates subcellular proteostasis.

Introduction

Protein homeostasis, hereafter proteostasis, is defined as the synthesis of proteins by translating genetic information, encoded in form of mRNA, into a sequence of amino acids and their regulated degradation. This intimate ying-yang balance between newly synthesized proteins

and protein degradation is tightly regulated in all organisms, in order to develop or respond to several environmental stimuli (Jayaraj et al., 2020; Orosa et al., 2020; Sampaio-Marques and Ludovico, 2018). Various perturbations can alter this equilibrium, leading to proteotoxic stress by disruption of normal proteostasis. This alteration can ultimately result in irreversible cellular damage due to the accumulation of aberrant proteins, an outcome known as proteotoxicity. Perturbations resulting in proteotoxic stress can range from ageing to pathological diseases such as Parkinson and Alzheimer as well as infection by pathogens (Jayaraj et al., 2020; Langin et al., 2023). The latter is a consequence of the onset and maintenance of defense responses during microbial infections and microbes' ability to manipulate proteostasis for their own benefit (Langin et al., 2023; Langin et al., 2020).

To mitigate deleterious effects due to excessive proteotoxic stress, cells employ various protein quality control machineries. Strikingly, the response to proteotoxic stress is often controlled by intricate regulatory feedback loops influenced by proteotoxic stress itself. One of the major protein quality control machineries across the tree of life is the ubiquitin-proteasome system (UPS). The ubiquitin-proteasome system controls proteostasis through selective elimination of defective proteins as well as short-lived regulatory proteins (Raffeiner et al., 2023). Selective protein degradation by the proteasome proceeds from the ligation of ubiquitin proteins to a lysine residue within specific target proteins via the concerted action of E1, E2, and E3 enzymes. The ubiquitinated target is then recognized by the 26S proteasome for degradation. The 26S proteasome itself is a conserved 2.5 MDa ATP-dependent protease complex composed of a 20S core protease (CP) capped by 19S regulatory particles (RPs), that assists in ubiquitin recognition and target protein unfolding. Recent findings highlight that the proteasome is a highly dynamic structure, as more than 40 subunits participate in forming the 26S proteasome. Changes in the subunit composition or the association of the 20S CP with other adaptors drive flexibility of the 26S proteasome which can help to cope with proteotoxic stress (Albert et al., 2020; Colberg et al., 2020; Peters et al., 2013; Tanaka et al., 2012). To guarantee this high degree of structural flexibility and to immediately react to proteotoxic stress, all the constituents of the 26S proteasome are under tight transcriptional control.

All eukaryotic kingdoms possess transcription factors (TFs) required for proteasome genes transcriptional activation (Marshall and Vierstra, 2019). Yeast utilizes the C2H2 zinc-finger TF Rpn4, mammals the bZIPs (Basic Leucine Zipper) Nrf1/2 and plants the pair of NACs (NAM, ATAF and CUC) NAC53/NAC78 as a conserved mechanism to cope with proteotoxicity

although all TFs are evolutionary distinct. In yeast and animal systems, the proteasome activators Rpn4 and Nrf1/2 have been shown to be UPS targets (Radhakrishnan et al., 2014; Sha and Goldberg, 2014; Steffen et al., 2010; Ulasov et al., 2022; Xie and Varshavsky, 2001; Xie, 2001). Rpn4 and Nrf2 are degraded in the cytosol while Nrf1, a tail-anchored (TA) protein, is subjected to endoplasmic reticulum-associated degradation (ERAD). In the context of exceeded proteasomal capacity, hereafter proteasomal stress, their degradation is impaired, leading to their stabilization and subsequent nuclear translocation for proteasome gene activation (Marshall and Vierstra, 2019). This transcriptional activation triggered by Rpn4 and Nrf1/2 is mediated through binding of, respectively, the proteasome-associated control element (PACE, [(A/G)GTGGC)]) or antioxidant response element (ARE, [(A/G)TGACTCAGC] (Baird et al., 2017; Mannhaupt et al., 1999; Shirozu et al., 2015; Xie and Varshavsky, 2001). This mechanism constitutes a negative feedback loop which allows systematic maintenance of proteasome homeostasis. In plants, NAC78 has been shown to mediate transcriptional activation of proteasome promoters through association with the proteasome regulatory cis element (PRCE, [TGGGC], (Nguyen et al., 2013). In addition, loss of the NAC53/78 TF pair rendered plants hypersensitive to proteasome inhibition due to its incapacity to activate proteasome genes expression (Gladman et al., 2016). Therefore, a similar proteasome regulatory feedback loop has been proposed in plants (Marshall and Vierstra, 2019); however, to date, no evidence supports NAC53/78 proteasomal degradation.

Given the importance of proteasomal degradation in various cellular pathways, from cell cycle to immune response (Langin et al., 2023; Ma and Liu, 2010; Wang et al., 2008; Wang et al., 2010), it appears that the autoregulatory feedback loop is a central mechanism to precisely integrate and coordinate stress responses through proteotoxic stress sensing. Indeed, a growing body of evidence suggests that localized proteotoxic stress in compartments and organelles causes the activation of respective proteasome-mediated degradation pathways to release the stress. These mechanisms include ERAD, Endosome/Golgi-associated degradation (EGAD), mitochondria-associated degradation (MAD) and chloroplast-associated degradation (CHLORAD) (Christianson and Ye, 2014; Fonseca and Carvalho, 2019; Liao et al., 2020; Ling et al., 2019). This implies a multi-layered role of the proteasome in governing subcellular proteostasis. This aspect is particularly relevant for semi-autonomous organellar nuclear-encoded proteins, as their regulation also involves cytosolic proteasomal degradation prior to organellar import (Bragoszewski et al., 2017; Hristou et al., 2020). In turn, perturbations in the turn-over of such proteins can lead to proteasomal stress. Indeed, Rpn4 is activated by mitochondrial precursor protein accumulation to likely upregulate the proteasome for removal

of precursor proteins (Kramer et al., 2021). While for Nrf1/2 similar mechanisms remain elusive, Nrf2 is activated upon mitochondrial stress and activates mitochondrial biogenesis and precursors import (Gureev et al., 2019). This places the evolutionary distinct transcription factors Rpn4, Nrf1/2 and NAC53/78 into the spotlight: Are they the main communicators between organelles and the 26S proteasome to cope with proteotoxicity? As such, proteasome activators could act as gatekeepers of the communication between the nucleus and energy-producing organelles to maintain subcellular proteostasis. While to date it remains elusive whether proteasome activators might act as such communicators, it would constitute a direct way to coordinate 26S proteasome capacity and proteasome substrates to cope with proteotoxic stress. It is also unknown how different signals from various organelles and compartments are integrated to respond to overall proteotoxic stress.

Here we demonstrate that the plant proteasome autoregulatory feedback loop, driven by the proteasome activators NAC53/78, functions as signal integrators by controlling the intracellular communication between the nucleus and the chloroplast during proteotoxic stress. We show that NAC53/78 are short-lived proteins regulated by the ERAD machinery through a mechanism we termed ER-Anchored-Protein Sorting (ERAPS). At steady-state conditions NAC53/78 are degraded via the HRD1-CDC48 axis. In contrast, proteotoxic stress caused by pathogenic infection or pharmacological drug treatments stabilizes both transcription factors, leading to their ERAPS-dependent nuclear translocation and subsequent transcriptional reprogramming. We identified that NAC53/78 coordinate the transcriptional activation of proteasome genes and repression of photosynthesis associated nuclear genes (PhANGs) through association with a conserved PRCE-like cis-element. Strikingly, we have found that the proteasome autoregulatory feedback loop is essential to maintain normal response to subcellular proteostasis perturbation. Ultimately, we identified that the transcriptional signature coordinated by NAC53/78 is a general feature in context of biotic interactions as wells as in response to various developmental cues. Taken together, our findings provide a new conceptual framework, in which an autoregulatory feedback loop shapes the response to environmental stress: the integration of signals from different organelles and the role of proteasome activators as gatekeepers of organelle communication constitutes a novel mechanism for ensuring the global surveillance of cellular proteostasis in photosynthetic tissues.

138 **NAC53/78 are central integrators of various proteotoxic stress conditions**

139 Proteotoxicity is triggered by a wide range of physicochemical stresses. The induced
140 proteotoxic stress is often due to a perturbation of local subcellular proteostasis. For instance,
141 damage in energy-producing organelles such as chloroplast and mitochondria often lead to
142 accumulation of proteins that are not imported into these organelles (Hristou et al., 2020;
143 Kramer et al., 2021). How such signals from different cellular compartments are integrated is
144 still not understood. Thus, we hypothesized that proteasome activators might play a role in
145 integrating signals from different locations. To test our hypothesis, we subjected the double
146 mutant *nac53-1 78-1,* known to be hypersensitive towards proteasome inhibition (Gladman et
147 al., 2016), to various treatments previously reported to induce proteotoxic stress through
148 specific mechanisms. We inhibited the proteasome (BTZ, (Gladman et al., 2016) and the
149 ubiquitin-dependent segregase CDC48, a central player of multiple associated-degradation
150 pathways (CB-5083, (Li et al., 2022; Marshall et al., 2019), and induced the ER unfolded
151 protein response (DTT, TM, (Pastor-Cantizano et al., 2020). Additionally, we targeted semi-
152 autonomous organelles such as chloroplasts and mitochondria (Lin, Cml and MV (Li et al.,
153 2022; Wu et al., 2019), and the cytosolic chaperone Hsp90 that is essential for the organellar
154 import of chloroplastic/mitochondrial precursors or proteasomal degradation of these
155 precursors (GDA, (Wu et al., 2019). Ultimately, we used pathogenic infection with the bacterial
156 strain *Pseudomonas syringeae pv. tomato DC3000* (*Pst*), known to impact cellular proteostasis
157 through multiple mechanism notably via direct proteasome targeting (Üstün et al., 2016)
158 (**Figure 1A**).

159 Consistent with previous studies, BTZ treatment led to *nac53-1 78-1* hypersensitivity resulting
160 in a complete growth defect. Similarly, CDC48 inhibition resulted in a strong plant growth
161 defect (**Figure 1B**), supporting the importance of the proteasome activators in the context of
162 general proteotoxic stress, beyond direct proteasome targeting. Consistently, we observed
163 increased sensitivity of the double mutant to ER stress inducers DTT and TM (**Figure 1B**).
164 Strikingly, all other treatments resulted in *nac53-1 78-1* double mutant increased tolerance
165 compared to WT plants (**Figure 1B**). In accordance with the hypersensitivity towards
166 proteasome inhibition, bacterial infection also increased susceptibility of the *nac53-1 78-1*
167 compared to Col-0 plants (**Figure 1C**).

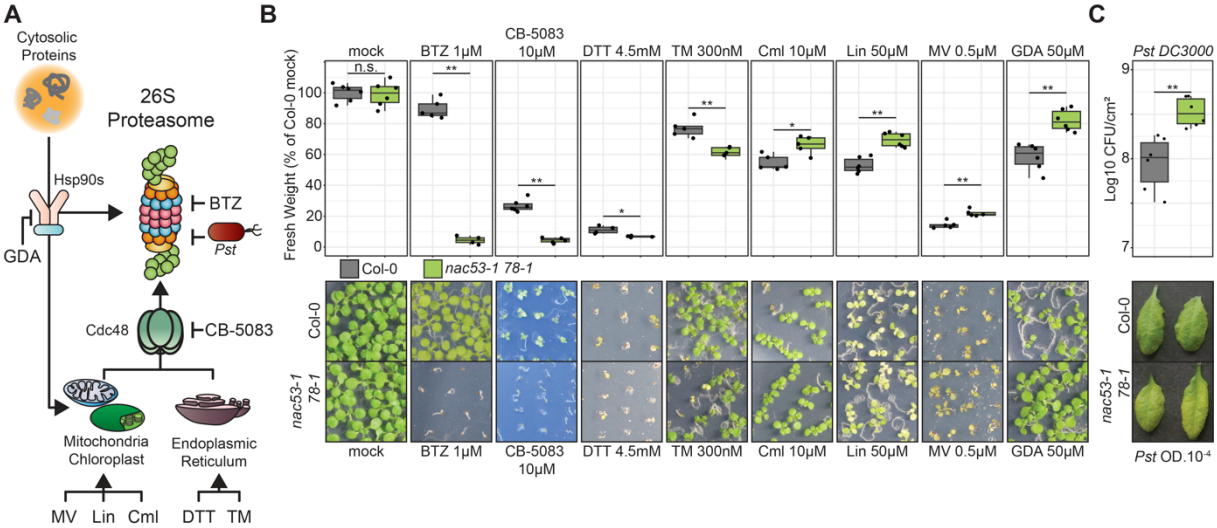

Figure 1. NAC53/78 are central integrators of various proteotoxic stress conditions.
(A) The role of the 26S Proteasome in degradation of proteins from distinct subcellular compartments. Prime site of action of the several treatments used in this study: Blunt head arrows indicate enzymatic activity suppression; pointed head arrows indicate trigger of substrate accumulation.
(B) Fresh weight of seedlings grown under the indicated treatments at 10-14 day after germination (dag). Fresh weight is expressed as a percentage of Col-0 mock conditions. Boxplots colors refer to the genotype. Statistical significance is assessed by a Wilcoxon-Mann-Whitney test (p values: n.s. > 0.05; * < 0.05; ** < 0.01). Every treatment has been repeated at least twice with similar results.
(C) Bacterial density in Log10 Colony-Forming-Unit (CFU) per leaf cm². Statistical significance is assessed by a Wilcoxon-Mann-Whitney test (p values: n.s. > 0.05; ** < 0.01). Boxplots colors refer to the genotype as in panel B. The treatment has been repeated three times with consistent results.
(B-C) Representative phenotypic pictures of Col-0 and *nac53-1 78-1* plants under several treatments are included.

Taken together this suggests that both proteasome activators are involved in general regulation of subcellular proteostasis. However, depending on the perturbation site, in the light of organellar stress, the response appears multi-layered. Overall, it suggests a precise subcellular regulation of NAC53 and NAC78 to adjust their impact on plant response to stress. But how do two transcription factors integrate different signals to have a global influence on the proteome during proteotoxic stress conditions?

NAC53/78 are part of an autoregulatory proteasome feedback loop

To elucidate how both TFs might integrate signals from different compartments and organelles, we aimed to decipher their regulation through interactome analysis. To this end, we generated transgenic plants expressing NAC53 or NAC78 tagged with eGFP at the N-terminus (N-ter), under control of the UBQ10 promoter (**Figure S1A**). Intriguingly, none of the generated lines displayed visible fluorescence under basal conditions (**Figure 2A**). Only upon proteasome inhibition with bortezomib (BTZ), GFP fluorescence was detected in nucleus (**Figure 2A**). These observations were confirmed by immunoblotting using an anti-GFP antibody (**Figure 2B**). Taken together, our results suggest that NAC53/78 are constitutively turned over by the proteasome implying the presence of an autoregulatory feedback loop.

199

200 To circumvent the short-lived feature of both NAC transcription factors in *A. thaliana*, and to
201 proceed with our interactome study, we used *Agrobacterium*-mediated transient expression in
202 *N. benthamiana* epidermal cells. Firstly, pUBQ10::GFP/RFP-NAC53/78 (hereafter referred as
203 sTag-NACs, **Figure S1A**) were transiently expressed in *N. benthamiana* to obtain details on
204 their subcellular localization in basal conditions. We could observe a fluorescence signal in
205 reticulated structures reminiscent of the endoplasmic reticulum (ER) as confirmed by co-
206 localization with an ER marker (mCherry-HDEL, **Figure 2C**). Such localization is consistent
207 with the presence of a predicted transmembrane domain (TM) at the C-terminus of both proteins
208 (**Figure S1A**). Due to this specific localization, we developed a second type of chimeric
209 constructs. We tagged the proteins at both ends including a mCerulean3 (CFP) at the N-ter and
210 a mCherry (RFP) at the C-terminus (C-ter), after the TM. These constructs were expressed
211 under regulation of a tandem *Lotus japonicus UBQ1* promoter to obtain stronger expression
212 (hereafter refers as dTag-NACs; **Figure S1A**; (Binder et al., 2014; Maekawa et al., 2008).
213 Interestingly, we could observe the CFP signal was mainly located in the nucleus while the RFP
214 remained strictly at the ER (**Figure 1D**). Both constructs appeared responsive to BTZ treatment
215 that led to stabilization of both NAC transcription factors in *N. benthamiana* strengthening our
216 findings that NAC53/78 are targets of the proteasome. (**Figure S1B and S1C**).
217 To decipher how both TFs might integrate signals from different compartments/organelles and
218 if an autoregulatory feedback loop governs their function, we performed immuno-Precipitation
219 (IP) followed by tandem Mass Spectrometry (MS/MS) with both constructs. We processed a
220 total of 4 IP-MS/MS conditions for both NACs among 2 experiments. We performed IP of sTag-
221 NACs in mock conditions and at 8 hours after bacterial infection, to induce proteoxic stress
222 (**Figure S1D**). In parallel, we performed IP of dTag-NACs enriching for the N-ter or C-ter end
223 of the proteins, which allowed us to characterize the interactome at a subcellular resolution
224 (**Figure S1E**). For our downstream analysis, we focused on the common interactors for both
225 NACs. Out of the 4 conditions we identified 245 unique *A. thaliana* orthologous proteins as
226 interactor candidates (**Figure 2E and Table S1**).
227 We first analysed the localization profile of NAC53/78 common interactome using the Gene
228 Ontology (GO) annotations for cellular components and the SUBA5 data base
229 (https://suba.live/). The GO analysis displayed enrichment for terms mainly associated with the
230 proteasome complex and plastid components (**Figure S1F**). This supports the importance of
231 the proteasome complex as a central hub in the NAC53/78 interactome. Investigating the

SUBA5 annotation of NAC53/78 interacting candidates, we observed a specific subcellular

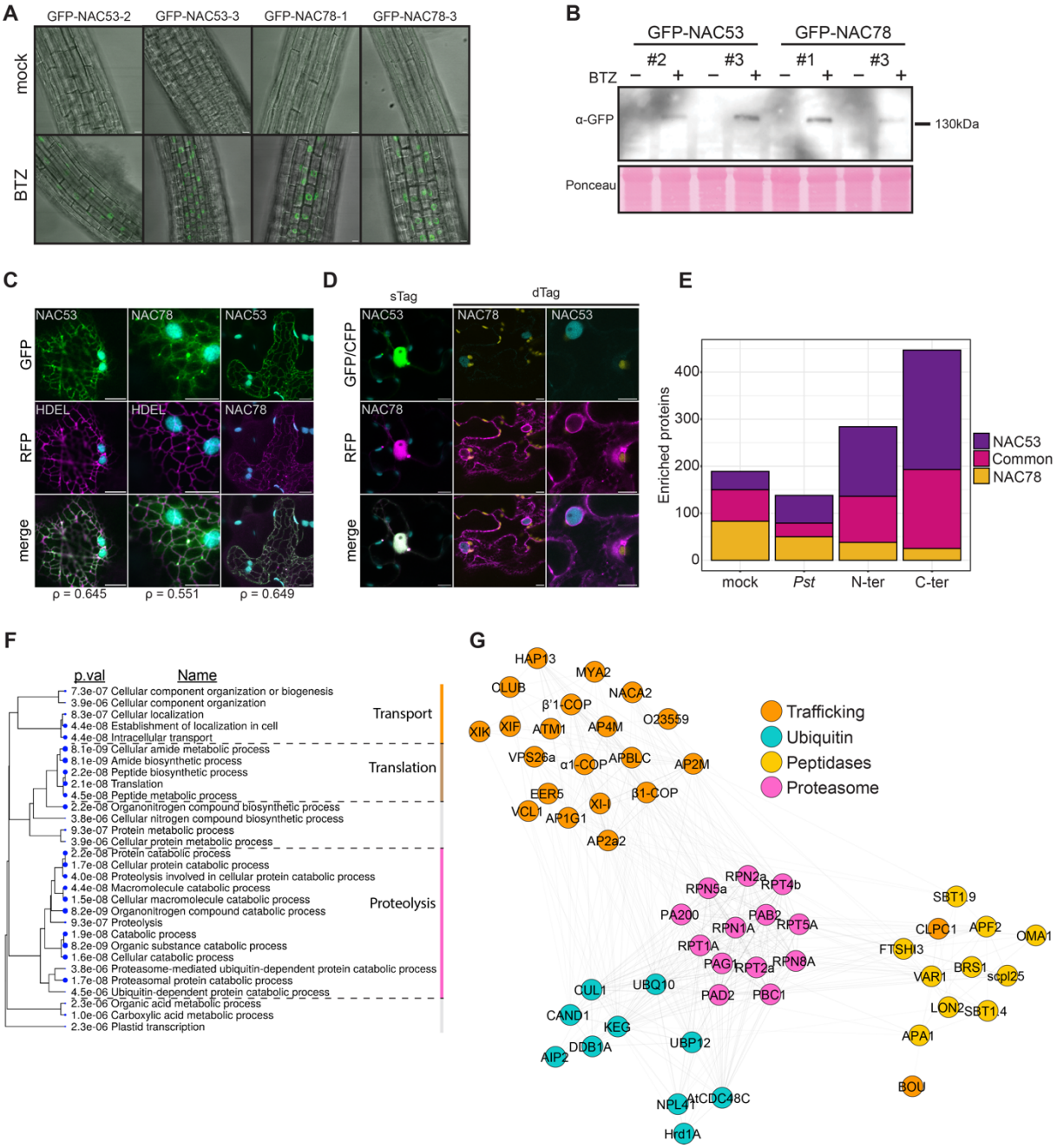

Figure 2. NAC53/78 are part of an autoregulatory proteasome feedback loop.
(A) Confocal microscopy pictures of roots of GFP-NAC53/78 *Arabidopsis thaliana* transgenics at 7dag exposed to mock or BTZ 10µM treatment for 3h. Treatments were repeated at least three times with similar observations.
(B) Immunoblot analysis against GFP on crude extract of seedlings related to panel A. Ponceau staining is used as loading control.
(C) Confocal microscopy pictures of transiently co-expressed sTag-NAC53/78 with prom35S::RFP-HDEL or together in *N. benthamiana* epidermis cells. Pearson index (ρ) represents co-localization index. Scale bars = 10µm
(D) Confocal microscopy pictures of transiently co-expressed sTag-NAC53/78 together or dTag-NAC53/78 alone in *N. benthamiana* epidermis cells. Scale bars = 10µm
(E) Bar plots representing the number of significantly enriched proteins in the 4 IP-MS/MS conditions for NAC53 only, NAC78 only and NAC53+NAC78 (Common).
(F) Cladogram of top 30 gene ontology (GO) terms for biological process (BP) enriched in the list of *A. thaliana* ortholog proteins found from NAC53/78 common interactome.
(G) Protein network of the interacting candidates related to the GO BP terms annotated as "Transport" and "Proteolysis" in panel F.

250 profile; we found enrichment for only 4 compartments: plastid, peroxisome, golgi, and
251 endoplasmic reticulum (**Figure S1G**). The latter is in accordance with the observed localization
252 (**Figure 2C**) and supports the importance of the ER-localization for the regulation of
253 NAC53/78. To understand how this regulation takes place, we further extended our analysis.
254 We performed GO analysis for biological processes and revealed that possible candidates were
255 enriched in proteins related to three main biological process: proteolysis, trafficking and
256 translation (**Figure 2F**). Based on our previous results we focused on the first two groups. We
257 extracted the corresponding proteins and performed a protein network analysis (**Figure 2G**).
258 This analysis highlighted the presence of numerous components of the ubiquitin-proteasome
259 system (UPS) (**Figure 2G; Figure S1H and S1I**); confirming the strong interplay of NAC53/78
260 with ubiquitin-dependent proteasomal degradation. Comparison of the protein enrichment level
261 in the several conditions revealed that association with the proteasome complex components
262 was strongly reduced by bacterial infection and mainly enriched when targeting the ER-
263 anchored end of the TFs (C-ter IP) (**Figure S1H**). It suggests that both proteasome regulators
264 escape proteasomal degradation in the context of proteotoxic stress and that ER is the major
265 site for their proteasomal removal. The latter was further supported by the presence of several
266 ERAD components in the interactome (**Figure 2G and S1I**). Additionally, both TFs were
267 associated with various trafficking components or peptidases (**Figure 2G**). Interestingly, the
268 affinity with most of these proteins was substantially differing based on the analysed condition
269 (**Figure S1J and S1K**). This indicates that the NAC53/78 interactome might involve further
270 regulatory layers dynamically shaped in response to proteotoxic stress.
271 Taken together our analysis confirmed that both proteasome activators are short-lived proteins
272 degraded by the proteasome. These findings reveal the presence of an autoregulatory feedback
273 in plants, similar to what has been found in yeast and animal (Marshall & Vierstra, 2019). In
274 addition, our interactome of NAC53/78 corroborates their role as integrators of subcellular
275 proteostasis perturbations.
276
277 **ER-Anchored Protein sorting (ERAPS) regulates the subcellular fate of NAC53 & NAC78**
278 Our analysis of the NAC53/78 interactome revealed that NAC53 and NAC78 associate with
279 proteins involved in the ubiquitin-proteasome system at the ER. Interestingly, among these
280 candidates, three belonged to the ER-Associated Degradation (ERAD) machinery, including
281 the membrane-bound E3 ligase HRD1 and the central component CDC48 (**Figure 2G and S1I**).
282 Given the ER localization of the TFs (**Figure 2C**) and the strong enrichment of proteasome

subunits in the C-ter IP-MS/MS condition (**Figure S1I**) we hypothesized that the turnover of both NAC TFs are regulated by ERAD.

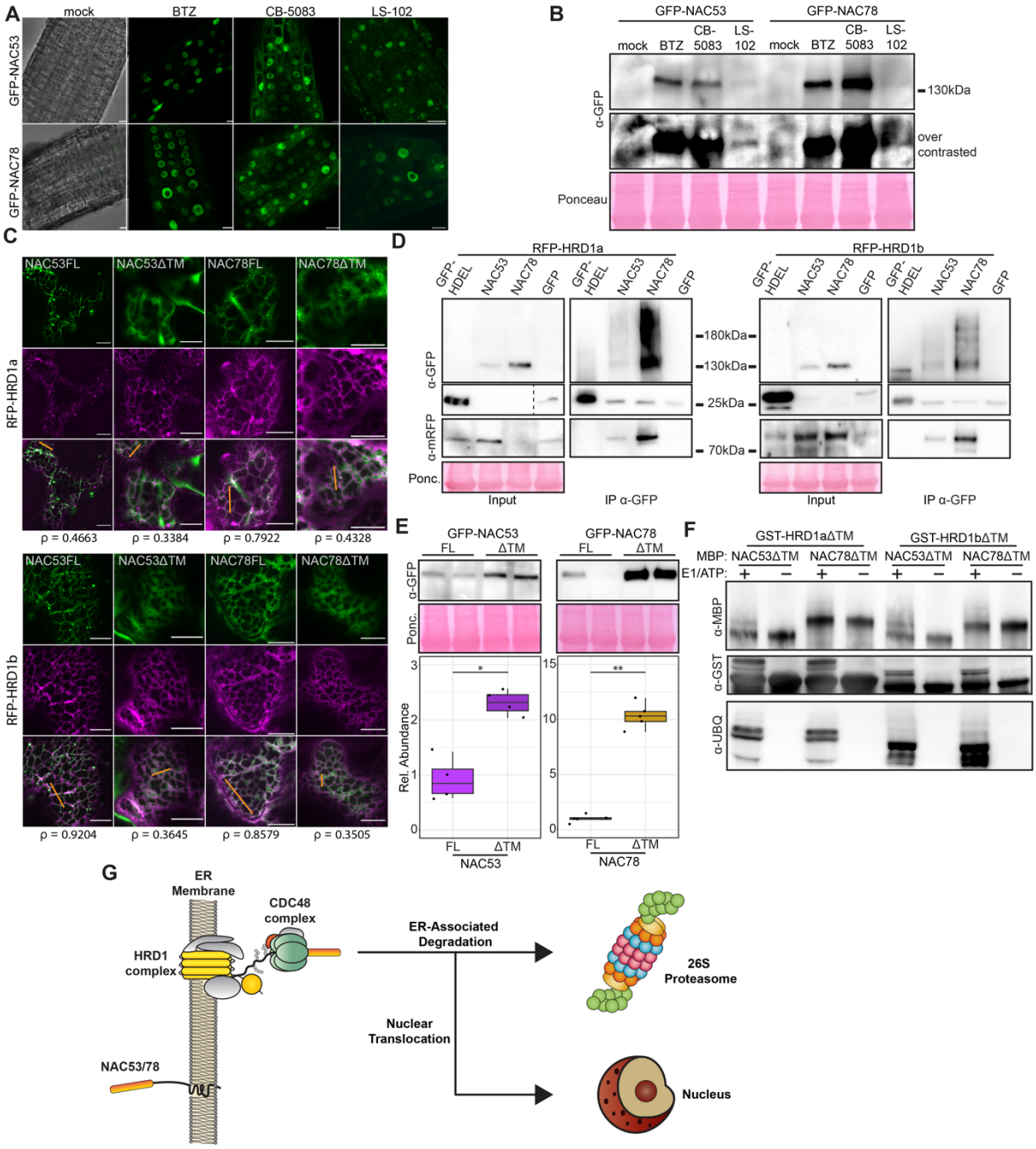

Figure 3. ER-Anchored Protein Sorting (ERAPS) coordinates the subcellular fate of NAC53 & NAC78.
(A) Confocal microscopy pictures of GFP-NAC53/78 expressing *A. thaliana* roots. 7 dag seedlings were exposed to mock treatment, BTZ 10µM, CB-5083 10µM or LS-102 100µM for 3h. The treatments were repeated at least three times with similar observations. Scale bars = 10µm
(B) Immunoblot against GFP on crude extracts of GFP-NAC53/78 *A. thaliana* adult plants infiltrated with mock treatment, BTZ 10µM, CB-5083 10µM or LS-102 100µM for 6h. Ponceau staining is used as loading control.
(C) Confocal microscopy pictures of *N. benthamiana* transiently co-expressing GFP-NAC53/78 full-length (FL) or deleted for the transmembrane domain (ΔTM) with RFP-HRD1a or RFP-HRD1b. Pearson index (ρ) indicates correlation index at the orange lines. Scale bars = 10µm
(D) Co-IP of RFP-HRD1a/b with GFP-NAC53/78. IP was performed with anti-GFP beads. GFP-HDEL and free-GFP were used as negative control. The experiment was repeated twice with similar results.
(E) Immunoblot against GFP on crude extract of *N. benthamiana* leaves transiently expressing GFP-NAC53/78FL or ΔTM. Ponceau was used as loading control. Boxplots represent the relative ΔTM abundance compared FL.

(F) *In vitro* trans-ubiquitination assays of GST-HRD1a/b against MBP-NAC53/78. Removal of E1 and ATP from the reaction was used as negative control. The experiment was repeated twice with similar results.
(G) Representation of the ER-Anchored Protein Sorting (ERAPS) mechanism. NAC53/78 are ER-anchored proteins recognized and ubiquitinated by the HRD1 complex. The CDC48 complex subsequently extracts NAC53/78 from the ER to mediate ER-Associated Degradation or allowing nuclear translocation in the context of proteasomal stress to mitigate proteotoxicity.

To investigate this possibility, we took advantage of previously characterized drugs: we treated the GFP-NAC53 and GFP-NAC78 transgenic lines with CB-5083 and LS-102, inhibitors of CDC48 and HRD1 proteins, respectively (Yagishita et al., 2012; Zhou et al., 2015). The effect of CB-5083 has already been characterized in plants (Li et al., 2022; Marshall et al., 2019), while LS-102 has not been characterized in plants to date. Our analysis revealed that LS-102 can efficiently inhibit both *A. thaliana* orthologs AtHRD1a and AtHRD1b *in vitro* (**Figure S2A and S2B**). Similar to BTZ treatment, CDC48 and HRD1 inhibition led to a stabilization of both proteins; visualized by confocal microscopy and through GFP immunoblotting (**Figure 3A and 3B**). Collectively, these results indicate that NAC53/78 are targets of ERAD. We next investigated whether NAC53 and NAC78 physically interact with both HRD1 isoforms. Transient co-expression of GFP-NACs with RFP-HRD1a/b revealed a strong association of NAC TFs with HRD1s at the ER, that was further confirmed by co-IP experiments (**Figure 3C and 3D**). The subcellular association was largely reduced upon deletion of the TM of both NAC TFs (ΔTM, **Figure 3C**). Interestingly, loss of ER association led to a strong stabilization of the proteins, supporting ERAD-dependent turn-over for both TFs (**Figure 3E**). These results support that NAC53/78 are targets of HRD1-mediated ubiquitination for proteasomal degradation.

To investigate whether HRD1s are indeed responsible for NAC ubiquitination, we performed *in vitro* ubiquitination assays using purified GST-HRD1a/b isoforms and MBP-NAC53/78 proteins. The assay revealed trans-ubiquitination of both NAC proteins in the presence of HRD1a and b that appeared in form of higher molecular weight bands of MBP-NAC proteins (**Figure 3E**). We could confirm the presence of ubiquitination marks at different sites via MS/MS analysis of the *in vitro* ubiquitination reactions (**Figure S2C and S2E**). In addition, ubiquitin marks were consistently inhibited by the addition of the inhibitor LS-102 to the *in vitro* ubiquitination assay (**Figure S2F**). The *in vitro* data was corroborated by identification of several ubiquitination sites on NAC53 and 78 in our *in vivo* IP-MS/MS analysis (**Figure S2D and S2E**). We confirmed *in planta* ubiquitination by performing ubiquitin IP on *N. benthamiana* leaves transiently expressing the dTag-NACs constructs (**Figure S2G**). Mutation of identified lysine residues substantially reduced the association with anti-ubiquitin beads *in planta* (**Figure S2H and S2I**). Altogether, our *in vivo* and *in vitro* analysis demonstrate that

336 NAC53 and NAC78 are directed to proteasomal degradation via ERAD through HRD1
337 ubiquitination.
338 During our analysis we could observe that NAC53/78 did not respond similarly to the tested
339 inhibitors. Indeed, upon BTZ or CB-5083 treatment, GFP signal in the transgenic lines
340 displayed different subcellular localization (**Figure 2A**). While BTZ led to a strong nuclear
341 localization; CDC48 inhibition by CB-5083 led to a nuclear localization and cytoplasmic dot-
342 like structures. To rule out the possibility of difference in drug potency, we treated plants with
343 higher concentration of both drugs. While double amount of BTZ resulted in a stronger nuclear
344 localization, an increase in CB-5083 concentration resulted in the accumulation of dot-like
345 structures (**Figure S3A**), which could be potential sites of CDC48/NAC association. Co
346 expression of *A. thaliana* CDC48 isoform (AtCDC48c) with both NACs revealed that CDC48
347 and NAC53/78 were able to associate in dot-like structures (**Figure S3B**). This indicates that
348 upon CDC48 inhibition in *A. thaliana*, NAC53/78 accumulate at sites of CDC48 action. Given
349 the role of CDC48 in retro-translocation of ER proteins to the cytosol, it could prevent
350 degradation of NAC53/78 but also perturb their subcellular sorting. To test this, we compared
351 the GFP signal intensity in the nucleus and cytoplasm upon BTZ and CB-5083 treatments
352 (**Figure S3C**). Upon CB-5083 treatment the mean GFP intensity per cell was generally higher
353 than upon BTZ (**Figure S3C**). This is consistent with a more diffuse localization of GFP signal.
354 However, we observed that upon BTZ treatment more than 50% of the signal was found in the
355 nucleus compared to 30% upon CB-5083 (**Figure S3D**). In addition, analysing the
356 nucleus/cytoplasm mean intensity ratio revealed that NAC53/78 concentrate 6 times more in
357 the nucleus upon BTZ compared to CB-5083 (**Figure S3E**). This analysis strongly suggests
358 that CDC48 is partially involved in the nuclear translocation of NAC53 and NAC78 in addition
359 to its role in proteasomal degradation.
360 In summary, we showed that the subcellular fate of NAC53 and 78 and hence the autoregulatory
361 feedback loop is coordinated by the ERAD machinery. The turnover of ER-anchored NACs
362 and their subsequent physiological impact is also the first example of the plant ERAD
363 machinery having a role beyond quality control of aberrant proteins. In parallel this mechanism
364 is responsible for their nuclear translocation (**Figure 3G**). Thus, we propose to refer to this
365 mechanism as ERAPS (ER-Anchored Protein Sorting).
366
367 **The transcriptional landscape of proteotoxic stress**

368 Having established that ERAPS is controlling the proteasome autoregulatory feedback loop in
369 plants, we wanted to understand why the *nac53-1 78-1* mutant is more tolerant to organelle-
370 directed proteotoxic stress while it is hypersensitive to general proteotoxic stress (**Figure 1B**).
371 To decipher the underlying mechanism, we utilized the fact that *Pseudomonas synringae*
372 infection is causing proteotoxic stress through the suppression of proteasome activity and broad
373 modification of chloroplast proteome (Littlejohn et al., 2021; Üstün et al., 2018; Üstün et al.,
374 2016). We first characterized the involvement of the proteasome autoregulatory feedback loop
375 during bacterial infection. Monitoring mRNA levels for both TFs genes, revealed an induction
376 of *NAC53* and *78* upon infection (**Figure 4A**). In addition, transcriptional activation of
377 proteasome genes was dependent on the presence of *NAC53* and *NAC78* WT alleles (**Figure**
378 **4B**). This was also consistent with an impaired protein accumulation of proteasome subunits in
379 *nac53-1 78-1* upon infection (**Figure 4C**). Finally, we observed that bacterial infection was
380 associated with the stabilization of NAC53 and NAC78 in *N. benthamiana* and *A. thaliana*
381 (**Figure 4E and 4F**). Altogether these results demonstrate that bacterial infection displays all
382 the features associated with proteotoxic stress that is dependent on the presence of both
383 proteasome activators. As such, this system is ideal to unveil the function of the proteasome
384 autoregulatory feedback loop in response to environmental perturbation.
385 To obtain a global idea on what else beyond the proteasome genes might be affected in *nac53-*
386 *1 78-1* plants we undertook a transcriptomic analysis. We first analysed the transcriptomic
387 profile of *nac53-1 78-1* infected with *Pst*. Interestingly, *nac53-1 78-1* displayed only 7
388 differentially expressed genes (DEGs) compared to Col-0 in mock (**Figure 4G)**, confirming
389 that NAC53/78 are mainly involved in stress responses (Seo et al., 2008). Comparing the *nac53-*
390 *1 78-1* to Col-0 in the context of bacterial infection revealed 945 DEGs. Strikingly, most of the
391 genes display a positive Log2FC (**Figure 4H**). This suggests that NAC53/78 are major
392 transcriptional repressors upon bacterial infection induced proteotoxic stress. We could confirm
393 that bacterial infection triggers a general NAC53/78-dependent transcriptional up-regulation of
394 proteasome related genes (**Figure S4A**). These results are in accordance with the involvement
395 of the proteasome regulatory feedback loop during infection. Further investigation of which
396 biological processes are enriched within the DEGs in our *nac53-1 78-1* transcriptome revealed
397 photosynthesis, glucosinolates, cell wall and auxin signalling as major terms (**Figure 4I**). To
398 refine our investigation and to include a broader view of the transcriptome landscape during
399 proteotoxic stress, we included two other datasets into our analysis. Firstly, we generated

another transcriptome in response to pathogenic bacteria, subjecting the *rpt2a-2* proteasome

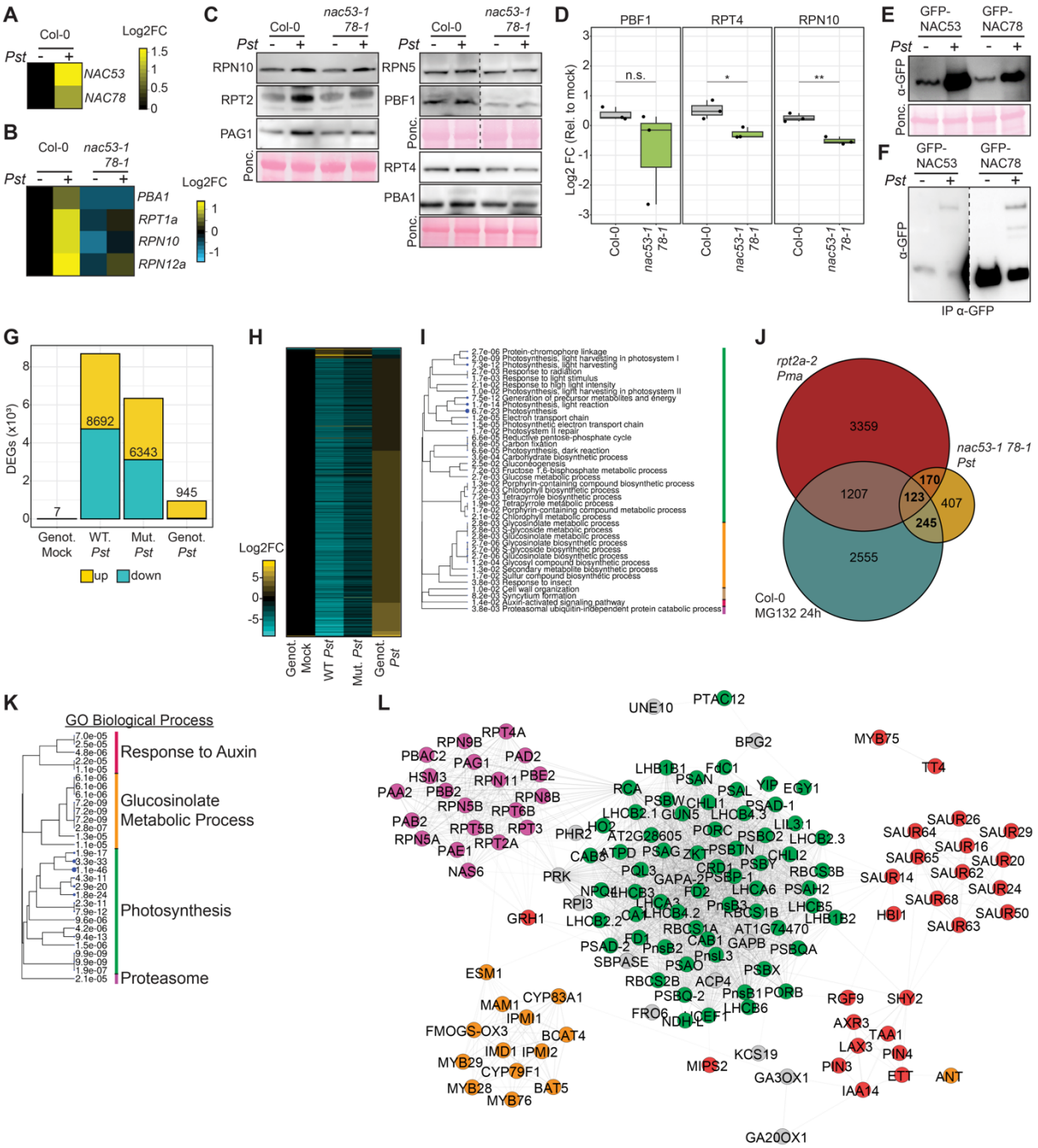

Figure 4. The transcriptional landscape of proteotoxic stress

(A) Log2FC mRNA levels of *NAC53* and *NAC78* transcripts after *Pst* infection of adult Col-0 plant leaves. The heatmap represent the mean of 4 biological replicates.

(B) Log2FC mRNA levels of 26S proteasome transcripts after *Pst* infection of Col-0 or *nac53-1 78-1* adult plant leaves. The heatmap represent the mean of 4 biological replicates. The experiment has been repeated 3 times with consistent results.

(C) Immunoblot against multiple 26S proteasome subunits on crude extracts of Col-0 or *nac53-1 78-1* adult plant leaves inoculated with *Pst* or mock solutions for 24h. Ponceau staining is used as loading control.

(D) Relative Log2FC abundance of representative 26S proteasome subunits in Col-0 or *nac53-1 78-1* adult plant leaves. The abundance is calculated relative to the mock conditions. Statistical differences are assessed via a Welch t.test (p values: n.s > 0.05, * < 0.05, ** < 0.01).

(E) Immunoblot against GFP on crude extract of *N. benthamiana* leaves transiently expressing GFP-NAC53/78 after mock treatment or *PstΔHopQ* infection for 8h. Ponceau staining is used as loading control.

(F) Immunoblot against GFP on extract of adult *A. thaliana* transgenics GFP-NAC53/78 subjected to mock treatment or *Pst* infection 8h by vacuum infiltration followed by IP with anti-GFP beads.

(G) Number of differentially expressed genes (DEGs) in the different conditions of the *nac53-1 78-1 Pst* RNAseq analysis. Total number of DEGs per condition is indicated. Colors indicate the proportion of DEGs up-regulated and down-regulated. DEGs are considered when |Log2FC| > 1.5. Genot. mock: *nac53-1 78-1* mock vs. Col-0 mock; WT *Pst*: Col-0 *Pst* vs. Col-0 mock; Mut. *Pst*: *nac53-1 78-1 Pst* vs. *nac53-1 78-1* mock; Genot. *Pst*: *nac53-1 78-1 Pst* vs. Col-0 *Pst*.
(H) Level of differential expression (Log2FC) of the 945 DEGs found in Genot. *Pst* (see panel G) for the several conditions analyzed.
(I) Cladogram of top 40 GO terms for BP enriched in the list of 945 DEGs. Colors represent broad GO clusters.
(J) Venn diagram representing the overlap between the 945 DEGs and DEGs from *rpt2a-2 Pma* (|Log2FC| > 0.5) or Col-0 MG132 24h (|Log2FC| > 0.5).
(K) Cladogram of top 30 GO terms for BP enriched in the list of 538 DEGs extracted from the combined analysis (panel J). For conciseness terms are hidden and grouped in 4 processes.
(L) Protein network of the genes from the 945 DEGs list related to the GO BP terms from panel K. Node colors refers to the 4 GO clusters from panel K.

mutant to *Pseudomonas syringae pv. maculicola* (*Pma*) infection. Contrary to *nac53-1 78-1,* this genotype displayed 251 DEGs in mock conditions (**Figure S4B**); indicating a basal stress response, including upregulation of proteasome genes, consistent with previous report (Lee et al., 2011). Upon infection we observed a large transcriptome variation compared to WT plant; with 981 DEGs identified specific to *rpt2a-2 Pma* condition (**Figure S4B and S4C**). Analysing the transcriptomic response of the proteasome complex, we found that most of the genes were further activated in response to infection in *rpt2a-2* background (**Figure S4D**). Interestingly, beyond terms associated with the proteasome, GO analysis on the 981 DEGs revealed others enriched process overlapping in both, *nac53-1 78-1* and *rpt2a-2*, transcriptomes (**Figure 4I and S4G**). Secondly, we included a previously characterized transcriptome analysis on Col-0 plants upon MG132 treatments (Gladman et al., 2016). This led to three distinct proteotoxic stress transcriptomes induced by drugs, infection and/or genetic mutations.

The comparison of all three datasets allowed us to extract a core set of 538 DEGs present in the *nac53-1 78-1* dataset and one or both others (**Figure 4J, Table S2**). Strikingly, GO enrichment on this subset of genes revealed 4 distinct biological processes involved (**Figure 4K**). Extracting the genes associated with these processes from the *nac53-1 78-1* 945 DEGs, we could define the core transcriptional network associated with proteotoxic stress (**Figure 4L**). This network is comprised of 4 modules: the proteasome genes, a major cluster of Photosynthesis associated nuclear genes (PhANGs), glucosinolate and auxin signalling pathways (**Figure 4K and 4L**). Analysing the transcriptional profile of the several clusters we identified interesting patterns (**Figure S4F**). While the proteasome cluster was present in all three datasets (**Figure S4C and S4F,** (Gladman et al., 2016), the glucosinolate related cluster was infection specific and the auxin cluster was found only in *nac53-1 78-1 Pst* and MG132 24h (**Figure S4H**). This further emphasized the specificity and complexity of the proteotoxic stress response. The photosynthesis cluster was found in significant proportions in all three datasets with 68 DEGs for *nac53-1 78-1 Pst*, 23DEGs for *rpt2a-2 Pma* and 57DEGs for MG132

458 24h (**Figure S4H, Table S2**). This suggests that PhANGs transcriptional repression is a
459 recurrent response to proteotoxic stress. Strikingly, similar to the transcriptional response of
460 proteasome genes, the differential expression of the other clusters is also happening in opposite
461 manner in *nac53-1 78-1 Pst* compared to *rpt2a-2 Pma* or MG132 24h (**Figure S4H**). It shows
462 that the observed transcriptional response is not due to an indirect effect of dysfunctional
463 proteasome in *nac53-1 78-1* background as our previous results could have suggested.
464 Altogether our analysis revealed a so far unidentified link between NAC53/78 and the
465 transcriptional regulation of PhANGs in response to proteotoxic stress.
466
467 **NAC53 and NAC78 coordinate the regulation of proteasome and photosynthesis gene**
468 **expression through the same cis-element**
469 To identify whether NAC53/78 mediate a link between proteasome activation and repression
470 of photosynthesis, we hypothesized NAC53/78 can act as novel repressors of PhANGs.
471 Previous reports have shown that NAC TFs are involved in transcriptional repression (Hao et
472 al., 2010; Shih et al., 2014). We therefore speculated PhANGs being direct targets of NAC53
473 and NAC78. This was also corroborated by the detailed analysis of distinct photosynthetic
474 processes: While many processes were downregulated in the proteotoxic stress core
475 transcriptome in the *rpt2a-2 Pma* and MG132 data sets, the absence of NAC53/78 had the
476 opposite effect, indicating a possible repression via the NAC53/78 module (**Figure S5A**). To
477 investigate a possible direct repression of PhANGs, we extracted the promoter regions of the 4
478 gene clusters from our transcriptional network (**Figure 4K and 4L**). Running enrichment
479 analysis for specific cis-element, we found that Proteasome and PhANGs promoters share a
480 similar cis-element characterized by the PRCE-like [TGGGC] motif, while the other clusters
481 did not (**Figure 5A**). This further supported the link between PhANGs regulation and the
482 proteasome regulatory feedback loop. In line with this, PRCE-like elements appeared
483 homogeneously distributed among PhANGs (**Figure S5B**). Additionally, analysis of the cis-
484 element position revealed a high frequency of occurrence and enrichment close to the
485 transcription starting site, similar to proteasome promoters (**Figure S5B and S5C**). We then
486 extracted two candidates' regions from LHCa3 and PSAD1 promoters (**Figure 5B**),
487 respectively members of the light harvesting complex I and photosystem I (**Figure S5A,**
488 (Leister, 2003). Performing electromobility shift assay (EMSA), we could confirm NAC53 and
489 NAC78 were able to associates with these elements (**Figure 5C**). Consistently, this association
490 was dependent on the presence of their respective DNA recognition motif (**Figure 5C**).

Furthermore, we confirmed the TGGGC motif as being the driver of this association, as mutated

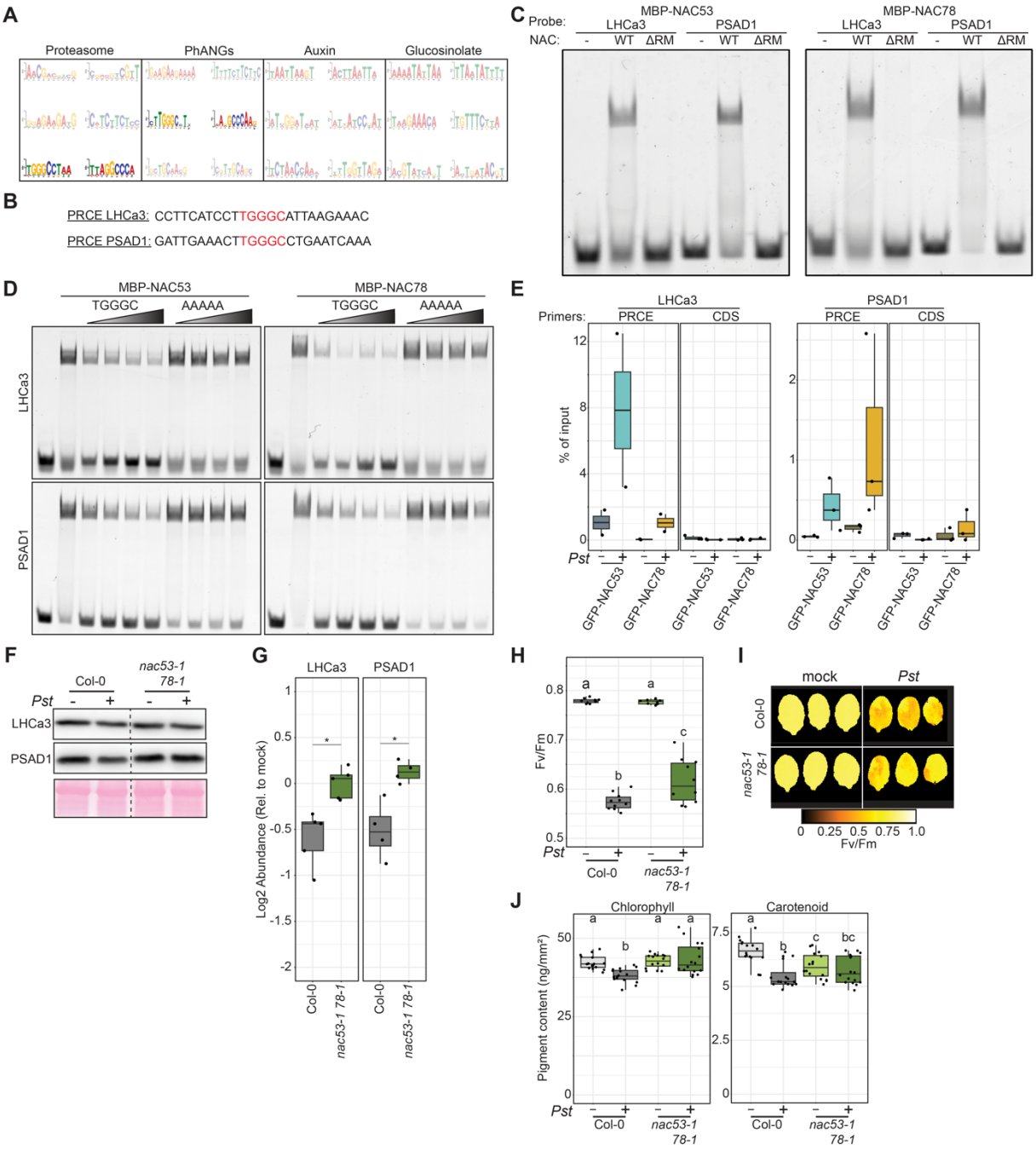

Figure 5. NAC53 and NAC78 coordinate the regulation of proteasome and photosynthesis gene expression through the same cis-element.

(A) Top 3 motifs found by STREME software in the promoter regions from the 4 network clusters (Figure 4L). PRCE-like elements from proteasome and PhANGs clusters are highlighted.

(B) 25bp region comprising the PRCE-like elements from LHCa3 and PSAD1 promoters used in this figure. The region corresponds to the probe sequence used in panel C and D. The PRCE is highlighted in red.

(C) Electro-Mobility Shift Assay (EMSA) of MBP-NAC53/78 with LHCa3/PSAD1 probes (see panel B). As a negative control, probes were incubated without MBP-NAC53/78 (-) or with MBP-NAC53/78 deleted for their DNA recognition motif (ΔRM). Experiment was repeated twice with similar results.

(D) EMSA competition assay of MBP-NAC53/78 association with LHCa3/PSAD1 probes. Competitor is applied at a concentration gradient (25X, 50X, 75X and 100X) indicated by the shade of grey. WT and mutated competitors are labelled TGGGC and AAAAA, respectively. Experiment was repeated twice with similar results.

(E) Boxplot representing association of GFP-NAC53/78 with LHCa3/PSAD1 PRCE in adult *A. thaliana* transgenics lines infected with *Pst* or mock for 8h after Chromatin Immunoprecipitation. The association is quantified as % of input and amplification of a region in the CDS is used as negative control.

(F) Immunoblot against mature PhANGs proteins in Col-0 or *nac53-1 78-1* adult plant leaves inoculated with *Pst* or mock solutions for 24h. Ponceau staining is used as loading control.
(G) Relative Log2FC abundance of PhANGs mature proteins immunoblotted in panel F. The abundance is calculated relative to the mock conditions. Statistical differences are assessed via a Welch t.test (p values: n.s > 0.05, * < 0.05, ** < 0.01).
(H) Photosystem II (PSII) activity measurement on Col-0 or *nac53-1 78-1* adult plants inoculated with *Pst* or mock solutions for 24h. Letters indicate the statistical group assessed by pairwise Welch t.test (p value < 0.05). The experiment was repeated 3 times with consistent results.
(I) Representative pictures of measurements from panel I. Fv/Fm values are represented by false color as indicated by the color gradient legend.
(J) Total chlorophylls and carotenoids from Col-0 or *nac53-1 78-1* adult plant leaves inoculated with *Pst* or mock solutions for 24h. Letters indicate the statistical group assessed by pairwise Wilcoxon-Mann-Whitney test (p value < 0.05). The experiment was repeated 3 times with consistent results.

oligos were unable to outcompete the association of NAC53/78 with the probes (**Figure 5D**). To corroborate our findings *in vivo*, we performed chromatin IP followed by qPCR in the context of bacterial-induced proteotoxic stress (**Figure 5E**). As expected, we could see that bacterial infection triggers the association of both TFs to both promoter regions, confirming the direct targeting of NAC53/78 to PhANGs promoters. To assess the regulatory role of NAC53/78 on PhANGs promoter activity, we used the luciferase reporter system in protoplasts (Yoo et al., 2007). Our analysis revealed that the PSAD1 promoter activity was consistently repressed by NAC53 and 78, which did not occur in *nac53-1 78-1* mutant protoplasts (**Figure S5D**). Deletion of the PRCE motif in PSAD1 abolished NAC78-mediated repression, while led NAC53 to mediate an increase in promoter activity (**Figure S5E**). In contrast, LHCa3 promoter activity appeared to be rather induced by NAC53 and unchanged by NAC78 (**Figure S5D**), with NAC53-mediated activation dependent on the PRCE motif (**Figure S5E**). This difference might be due to the fact that both TFs are expressed without a TM domain, bypassing ERAPS, in a rather artificial system. To circumvent this problem, we analysed the gene expression of *LHCa3* and *PSAD1* in the transgenic NAC53 and 78 lines upon BTZ treatment. Proteasome inhibition in the transgenic NAC53 and 78 lines partially enhanced the repression of PhANGs, supporting the notion that NAC53/78 act as repressors of photosynthesis during proteotoxic stress (**Figure S5F**). In addition, both lines showed an increase in *PBA1* and *RPT2a* mRNA (**Figure S5G**), confirming that NAC53/78 can act concomitantly as transcriptional repressor and activator. These results confirmed the importance of the PRCE-like element in PhANGs promoters, suggesting that NAC53 and NAC78 possess the ability to modulate each other's activity and highlights the complexity of the NAC53/78-PRCE regulatory module mediating transcriptional repression and activation on distinct gene cluster.

As NAC53 and NAC78 can associate with the PRCE-like element in PhANGs promoters to dampen their transcriptional activity, it is likely that they act as novel repressors of photosynthesis. To confirm this hypothesis, we analysed the protein abundance of LHCa3 and

548 PSAD1 proteins in the context of bacterial infection (**Figure 5F and 5G**). Immunoblot revealed
549 that contrary to Col-0, infection induced reduction of photosynthesis-associated proteins
550 appeared less pronounced in the *nac53-1 78-1* background (**Figure 5F**). Semi-quantitative
551 analysis on several replicates confirmed this observation (**Figure 5G**). This confirms that the
552 observed transcriptional repression mediated by the NACs has a major impact on PhANGs
553 protein levels. To test if this protein pool perturbation would impact photosynthesis, we
554 monitored PSII activity during infection. We found that *nac53-1 78-1* displayed significantly
555 less PSII activity reduction compared to Col-0 (**Figure 5H and 5I**). In addition, when
556 monitoring photosynthetic pigment content in the same context, we observed that total
557 chlorophyll and carotenoid content reduction during infection occurred to a lesser extent in the
558 *nac53-1 78-1* background (**Figure 5J**). Consistently with these findings, subjecting the
559 NAC53/78 transgenics to constant proteasome inhibition resulted in strong developmental
560 defect compared to WT (**Figure S5H and S5I**), suggesting that the role of NAC53/78 on
561 photosynthesis repression is not restricted to bacterial infection.
562 Altogether, we demonstrate the unique ability of NAC53 and NAC78 to mediate activation and
563 repression of target genes through the PRCE transcriptional module. This makes them novel
564 repressors of photosynthesis during bacterial infection-induced proteotoxic stress. It also might
565 explain our previous findings that the NAC mutant was more tolerant to organelle-directed
566 proteotoxic stress, suggesting that photosynthesis repression is a general feature of the
567 proteasome autoregulatory feedback loop to cope with proteotoxicity.
568
569 **The proteasome autoregulatory feedback loop monitors photosynthesis homeostasis**
570 **during stress responses**
571 Our results show that NAC53/78 co-regulate proteasome and PhANGs by recognizing the same
572 cis-element during bacterial infection induced proteotoxic stress. However, this feature does
573 not only occur during bacterial infection as the PhANGs repression was also observed when
574 proteasome was chemically inhibited (**Figure 4L, S5A, S5F and S5G**). Consistent with this,
575 we have observed that the *nac53-1 78-1* mutant also performed better when we perturbed
576 organellar proteostasis (**Figure 1B**). In addition, recent evidence suggests that loss of
577 proteasome function in a chloroplast import deficient mutant increased photosynthetic capacity
578 due to a lack of chloroplast precursor proteins degradation (Grimmer et al., 2020). Altogether,
579 this hints towards a general role of the proteasome activators NAC53/78 to co-ordinate
580 photosynthesis and proteasome homeostasis during proteotoxic stress.
581

582 To investigate to which extend NAC53/78 were involved in response to chloroplast
583 perturbation, we analysed the photosynthetic response of *nac53-1 78-1* plants upon Bortezomib
584 and Lincomycin treatments. Our analysis revealed that the decrease in pigment content was
585 impaired in *nac53-1 78-1* in comparison to Col-0 plants upon BTZ and Lincomycin treatment
586 (**Figure 6A**). Consistent with this, repression of PhANGs was less pronounced in the double
587 mutant (**Figure 6B**) which resulted in a higher photosynthetic activity in *nac53-1 78-1* upon
588 Lin treatment (**Figure S6A**).
589 To directly study the involvement of the proteasome autoregulatory feedback coordination of
590 cellular proteostasis and photosynthesis, we decided to analyse the central ERAPS regulators
591 HRD1a/b utilizing the inhibitors that were used in the NAC double mutant phenotyping (**Figure**
592 **1**). Proteasome inhibition rendered the *hrd1a 1b* more tolerant in comparison to Col-0 (**Figure**
593 **6C**), which is consistent with its role in negatively regulating NAC53/78 stability (**Figure 3G**).
594 In contrast, all other tested drugs or bacterial infection rendered the *hrd1a 1b* mutant more
595 susceptible (**Figure 6C and 6D**). The reduced growth of *hrd1a 1b* upon chloroplastic
596 perturbations (Cml and Lin) are consistent with our previous results (**Figure 1B**), as
597 stabilisation of NACs would lead to increased repression of PhANGs and growth reduction
598 (**Figure S5A, S5H and S5I**). The impaired performance of *hrd1a 1b* upon CDC48 inhibition,
599 pathogen infection or ER stress induction might be due to the general function of HRDs in
600 ERAD (Chen et al., 2016) and thus appear to be pleiotropic. Consistent with this idea, analysis
601 of the photosystem II activity revealed a stronger reduction in the *hrd1a 1b* double mutant
602 (**Figure S6B**) upon infection corroborating our findings that ERAPS coordinate proteasome
603 and photosynthesis through NAC53/78 stability. In addition, these data suggest that organellar
604 perturbation would lead the NAC53/78 activation. Indeed, subjecting GFP-NACs transgenics
605 to several organellar perturbators led to stabilization and nuclear localization of both TFs
606 (**Figure S6C**). Taken together our analysis illustrates the importance of the proteasome
607 autoregulatory feedback loop in maintaining the fine equilibrium of proteostasis to ensure
608 normal response to proteotoxic stress.
609 We found that regardless the genetic mutations impacting the feedback loop, the plants
610 displayed an increased susceptibility to bacterial infection (*rpt2a-2*, Üstün et al. (2016)). This
611 finding demonstrates the importance of this mechanism in agronomically important context and
612 raises the question if the autoregulatory feedback loop is involved in other conditions. To

answer this, we performed a large-scale transcriptomic analysis using the recently developed

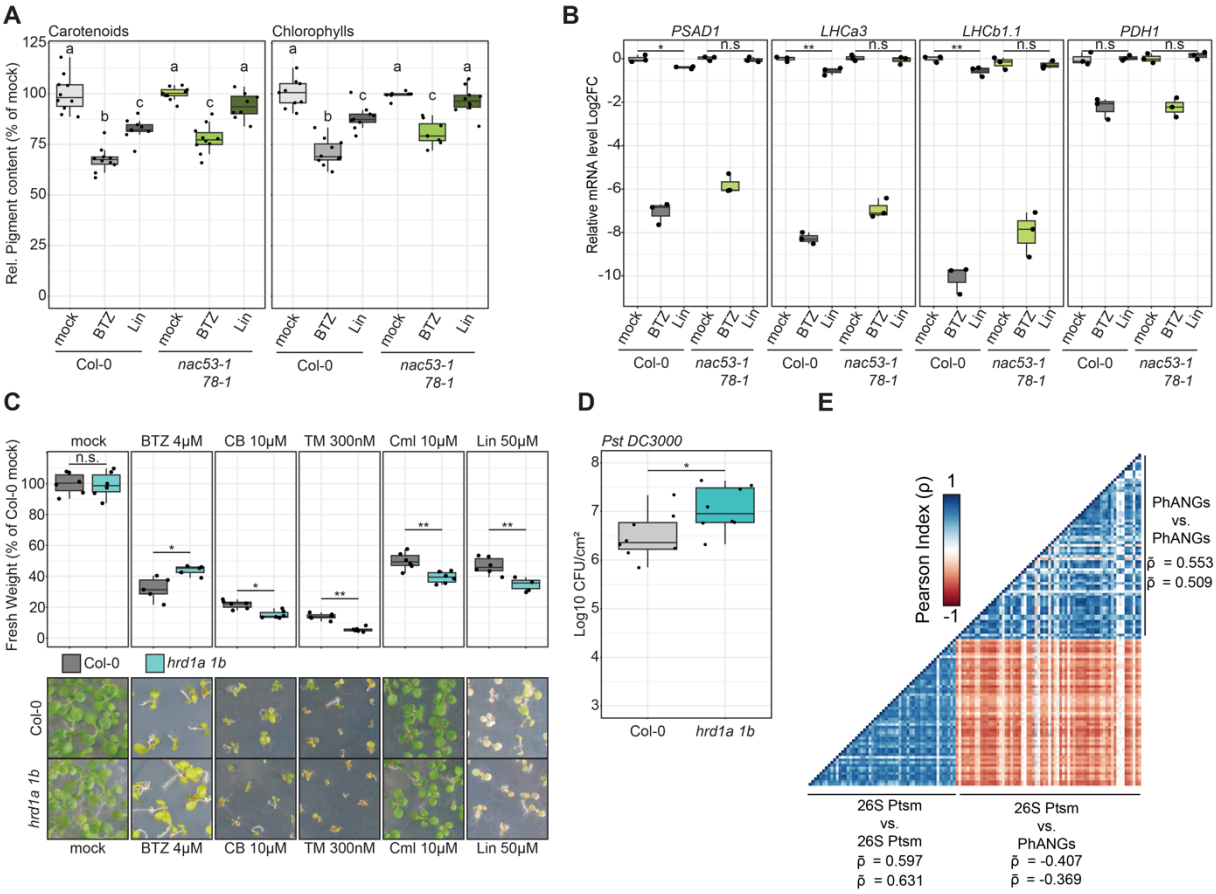

Figure 6. The proteasome autoregulatory feedback loop monitors photosynthesis homeostasis during stress responses

(A) Photosynthetic pigment content from Col-0 or *nac53-1 78-1* adult plant leaves infiltrated with Lin 200µM, BTZ 2µM or mock solutions for 24h. Content is expressed in percentage relative to Col-0 mock. Letters indicate the statistical group assessed by pairwise Wilcoxon-Mann-Whitney test (p value < 0.05). The experiment was repeated 3 times with consistent results.

(B) Log2FC mRNA level of the indicated transcripts in Col-0, *nac53-1 78-1* adult plants leaves Lin 200µM, BTZ 2µM or mock solutions for 24h. Log2FC is calculated from Col-0 mock and *PDH1* is used as negative control. Statistical differences are assessed with a Welch t-test (p values: n.s. > 0.05, * < 0.05, ** < 0.01). The experiment was repeated twice with consistent results.

(C) Fresh weight of seedlings grown under the indicated treatments at 10-14 day after germination. The fresh weight is represented as a percentage of Col-0 mock conditions. Letters indicate the statistical groups assessed by pairwise Wilcoxon-Mann-Whitney test (p value < 0.05). Every treatment has been repeated at least twice with consistent results. Representative phenotypic pictures are included.

(D) Bacterial density shown as Log10 Colony-Forming-Unit (CFU) per leaf cm² in Col-0 and *hrd1a hrd1b* plants. Statistical significance is assessed by a Welch t-test (p values: * < 0.05). The experiment has been repeated three times with consistent results.

(E) Correlation heatmap of the 54 26S proteasome subunit genes and the expression of 68 PhANGs from publicly available 1223 RNAseq libraries identified in this study.

Arabidopsis RNAseq data base (Zhang et al., 2020). We first investigated the relationship of transcript abundance between the 54 genes encoding 26S proteasome subunits and the 68 PhANGs associated with proteotoxic stress (**Figure 4**). We first extracted 165 unique projects of interest (see Methods, **Table S3**) to perform a correlation analysis between mRNA abundance of individual genes from both clusters (**Figure 6E**). We could observe that genes within each

640 cluster displayed a strong positive correlation ($\rho \approx 0.6$ and $\rho \approx 0.5$ for 26S Proteasome and
641 PhANGs, respectively). Strikingly, analysing relationship between the two clusters showed a
642 significant negative correlation ($\rho \approx -0.4$). It demonstrates that both clusters are regulated in
643 opposite manner (**Figure S4H**) and that this is a general feature of stress responses. We
644 therefore refined our analysis to define the spectrum of conditions displaying this
645 transcriptional signature (see Methods). Thus, we extracted 43 projects in which 26S
646 Proteasome and PhANGs appear transcriptionally co-regulated (**Table S3**). From these 43
647 projects, 35 displayed an opposite regulation for 26S Proteasome and PhANGs mRNA level
648 (**Figure S6G**), confirming that both clusters undergo recurrent contrasting co-regulation.
649 Looking at the conditions related to these datasets revealed that bacterial, oomycete infection
650 or elicitation, led to a negative correlation of proteasome gene expression and PhANGs
651 expression. This is in line with our previous observation using *Pst* infection. Beyond biotic
652 stress, our analysis unveiled several other contexts, such as cold, dark and drought treatments
653 as factors triggering this negative correlation (**Figure S6G**). Furthermore, we found that
654 treatment with trans-chalcone a phytotoxin notably causing shoot bleaching (Diaz-Tielas et al.,
655 2019) also resulted in a similar response. In addition to abiotic stress, nutrient stress and
656 circadian rhythm triggered the same transcriptional signature. It suggests that coordination of
657 PhANGs/Proteasome is not only a feature of plant stress response but also a characteristic of
658 developmental processes which is additionally mirrored in hormone treatments such as SA and
659 Auxin (**Figure S6G**).
660 Taken together, we found that the role of NAC53/78 in repression of photosynthesis is a general
661 feature of proteotoxic stress at any subcellular level. We discovered that the coordination of
662 proteasome activation and PhANGs repression is a key feature of the *Arabidopsis thaliana*
663 transcriptome in response to multiple biotic, abiotic, and developmental cues. Given the
664 conserved nature of the autoregulatory feedback loop in yeast, plants and animals, our findings
665 bear the potential that proteasome activators are general gatekeepers of the interplay between
666 the proteasome and energy metabolism across the tree of life.
667

668 **Discussion**

669 Understanding how eukaryotic organisms orchestrate proteostasis in a complex
670 compartmentalized cellular environment is a long-standing question. Although the proteasome
671 can degrade proteins from different compartments and organelles, how these different
672 subcellular signals are integrated upon external cues and coordinated to maintain overall
673 proteostasis was unknown.

Here, we have characterized that the proteasome autoregulatory feedback loop, involving the transcriptional NAC53/78-PRCE module, acts as a gatekeeper to facilitate the communication between the triangle chloroplast-proteasome-nucleus during proteotoxic stress (**Figure 7**).

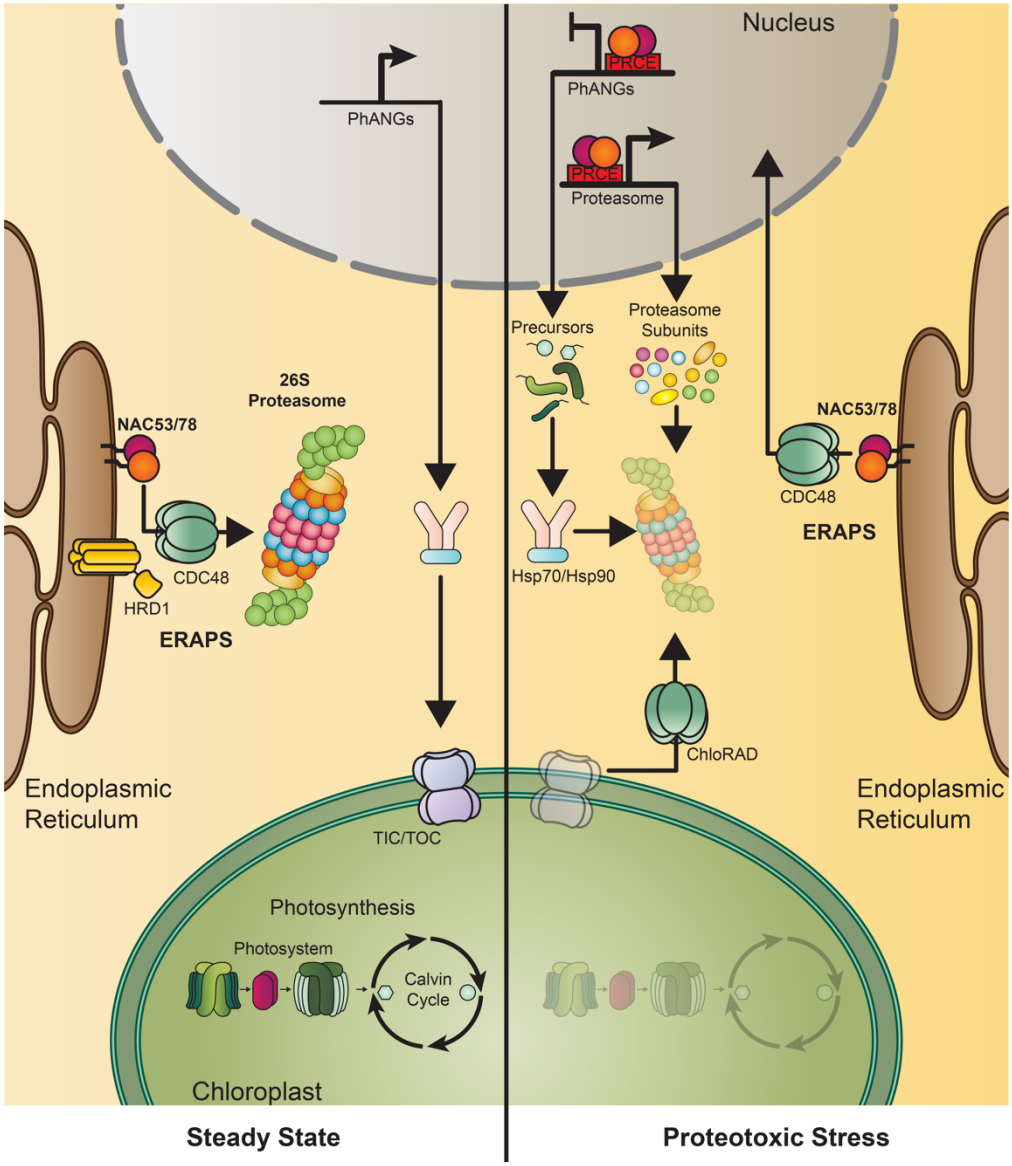

Figure 7. ER-anchored protein sorting (ERAPS) controls the fate of two proteasome activators for intracellular organelle communication during proteotoxic stress.
In steady state conditions, the ER-anchored protein sorting system (ERAPS) promotes the constitutive degradation of NAC53/78 via the 26S proteasome. Meanwhile, PhANGs expression is activated and subsequent chloroplastic import permits the maintenance of active photosynthesis. Upon proteotoxic stress, the chloroplast import machinery is targeted for proteasomal degradation. This leads to an accumulation of PhANGs precursors which are therefore subjected to proteasomal degradation, inducing proteotoxicity. Thus, to avoid proteotoxicity, the ERAPS system facilitates the nuclear translocation of NAC53/78, to activate the production of a new proteasome complex and to repress PhANGs expression to mitigate substrate accumulation.

We have shown that the trade-off between proteasome activation and photosynthesis downregulation is activated in response to various environmental and developmental cues

692 including disease. Using bacterial infection induced proteotoxic stress, we have identified
693 ERAPS as the key regulatory node of this feedback loop and how the latter shapes and maintains
694 subcellular proteostasis in plants. Considering that the autoregulatory feedback loop is
695 mechanistically conserved across kingdoms, similar control mechanisms of subcellular
696 proteostasis are possible in yeast and in animals (Marshall and Vierstra, 2019). While in yeast
697 the main proteasome regulator is the cytosolic TF Rpn4; in animal systems, SKN-1A/Nrf1 is
698 an ER-anchored protein which has also been shown to be subjected to ERAD (Radhakrishnan
699 et al., 2014; Ruvkun and Lehrbach, 2023; Steffen et al., 2010). It suggests further mechanistic
700 similarities between plant and animal systems, despite proteasome activators distinct
701 evolutionary origins, as our study demonstrates the importance of ERAPS for the subcellular
702 fate of NAC53/78, to a similar extend to what was reported for Nrf1 (Ruvkun and Lehrbach,
703 2023), emphasizing the conserved role ERAPS in regulating the proteasome activators.
704 However, our data might suggest that nuclear translocation of NAC53 and 78 is only partially
705 dependent on CDC48, as both NACs are still present in the nucleus upon CDC48 inhibition. In
706 addition, the phenotypes observed using the *hrd1a hrd1b* mutant and the localization of both
707 TFs upon LS-102 treatment suggest that HRD1-mediating ubiquitination is not strictly required
708 for NAC53/78 nuclear translocation. Thus, it is likely that the ERAPS system involves
709 alternative actors or other regulatory layers to mediate the transport of both TFs into the nucleus.
710 For instance, SKN-1A/Nrf1 TFs were reported to be targeted by the ubiquitin-dependent
711 DDI1/2 aspartyl-proteases for cleavage, downstream of their retro-translocation (Ruvkun and
712 Lehrbach, 2023). Although NAC53/78 are evolutionary distinct from SKN-1A/Nrf1 and do not
713 share the known DDIs cleavage site, we cannot exclude similar activation process due to the
714 presence of an ortholog, DDI1, in *A. thaliana* (Farmer et al., 2010). In addition, a recent report
715 has proposed a second ubiquitination step for Nrf1 in the cytosol which would facilitates DDI2-
716 mediated cleavage (Hu et al., 2023). The presence of cytosolic E3 in NAC53/78 interactome
717 could support similar mechanisms.
718 The ERAPS-dependent autoregulatory pathway proposed here would permit a rapid integration
719 of proteotoxic signals from various compartments. As such, it would allow the communication
720 between different organelles such as chloroplast or mitochondria with the nucleus, a process
721 referred as retrograde signaling, known as the modulation of nuclear encoded gene expression
722 in response of organellar proteostasis modification (Woodson and Chory, 2012). This
723 communication is essential to respond to sudden changes in the environment. As such,
724 retrograde signaling from mitochondria or chloroplast to the nucleus involves massive
725 transcriptional changes that in turn influence organelle function (Richter et al., 2023). Thus, it

726 requires tight transcriptional regulation to respond to signals from different organelles. Some
727 nuclear communicators have been identified to mediate retrograde signaling (Richter et al.,
728 2023). However, to date, transcription factors GLK1 and 2, are the only known PhANGs
729 activators (Waters et al., 2009), while putative repressors ABI4 and PTM could not be verified
730 as retrograde signaling components (Kacprzak et al., 2019; Koussevitzky et al., 2007; Page et
731 al., 2017; Sun et al., 2011). Here we have identified that plants have evolved a dual-regulatory
732 system through the proteasome autoregulatory feedback loop: the NAC53/78-PRCE module
733 acts as a novel retrograde signaling component, repressing PhANGs expression during
734 prolonged proteotoxic stress. By binding to the same cis-element the NAC53/78 module is able
735 to activate proteasome genes and repress PhANGs. In this scenario, (i) repression of PhANGs
736 by NAC53/78 may be a strategy to cope with the excess of precursor accumulation due to
737 proteasomal stress (**Figure 7**) which is corroborated by our findings that the *nac53-1 78-1*
738 mutant is more tolerant to photosynthesis stress and HSP90 inhibition which activate
739 NAC53/78 nuclear localization but also (ii) to counteract the overactivation of PhANGs by
740 GLK1 that is degraded by the proteasome (Tokumaru et al., 2017). Although, NAC TFs have
741 been reported to possess a repressor domain (NARD) (Hao et al., 2010), an intriguing question
742 remains: how are NAC53/78 acting as activators and repressors using the same cis-element?
743 Future investigations on this are necessary to improve our understanding how NACs activate
744 and repress gene expression simultaneously or in a concurrent manner to mediate retrograde
745 signaling.
746 In line with our findings, similar strategies to cope with the trade-off between proteasome
747 activation and energy producing organelles have been established in yeast for mitochondrial
748 associated proteins (Boos et al., 2019; Weidberg and Amon, 2018). In this case proteasome
749 activator Rpn4 is activated upon accumulation mitochondrial precursor protein accumulation
750 to turn on a second regulator Pdr3 which triggers the so called mitochondrial compromised
751 protein import response (mitoCPR) (Kramer et al., 2021). This rather constitutes an indirect
752 mechanism to transcriptionally repress the mitochondrial oxidative phosphorylation machinery
753 (OXPHOS). This implies a divergence between yeast and plants on subcellular proteostasis
754 coordination. It is tempting to propose these differences have emerged due to multicellularity
755 allowing an improved flexibility depending on the tissue or cell types. This hypothesis is
756 supported by the lack of the PRCE cis-element in the proteasome gene promoters of the
757 monocellular algae *Chlamydomonas reinhardtii* (Nguyen et al., 2013). In addition, we could
758 observe NAC53/78 activation in root cells, which lacks chloroplasts.. This observation further
759 supports the general function of the proteasome regulatory feedback loop in maintenance of

subcellular proteostasis upon stress, not limited to chloroplastic impairment. To our knowledge, a similar system has not been found in other multicellular organisms such as animals. However, the characterization of OXPHOS gene repression by ATFS-1 during mitochondrial unfolded protein response (Shpilka et al., 2021), the importance SKN-1A/Nrf1 upon oxidative stress and the role of Nrf2/Nrf1 in mitochondrial biogenesis and proteasome activation (Ruvkun and Lehrbach, 2023) strongly suggests a tight link between proteasome and mitochondrial proteostasis in animals. Interestingly, another NAC TF, ANAC017 was characterized to mediate mitrochondria-nucleus retrograde signaling (Ng et al., 2013). As NAC TFs are known to function as homo or hetero-dimers (Welner et al., 2016), it is tempting to speculate that the proteasome autoregulatory feedback loop involves additional NAC in concert with NAC53/78, or other TFs, orchestrating the specificity of the transcriptional response.

Various environmental perturbations impede the balance between protein translation, sorting and degradation resulting in proteotoxicity. This has a global effect on proteostasis, and as mounting evidence highlights a role for the proteasome in clearing organelle-associated proteins it is essential to decipher how signals from different compartments and organelles are integrated to maintain proteostasis and avoid proteotoxicity. As such, our findings here lay the foundation to study whether the role as communicators between organelles during proteotoxic stress is a common feature of proteasome activators in different kingdoms.

Acknowledgments

We thank Yasin Dagdas and Marja Timmermans for critical discussions during the thesis advisory committee meeting. We are thankful to Ophélie Léger and Paul Gouguet for stimulating discussions. We thank Nan Wang for technical advice on the Ch-IP procedure, Robert Morbitzer for technical support on the golden gate molecular cloning. We are grateful to Ana Gabriela Andrade-Galan and Lars Pospisil for technical support on the Photosystem II activity measurement. Stefan Bieker for the help with the computational analysis. We are thankful to Jos Schippers, Yasin Dagdas and Richard Vierstra for sharing published material. This work was supported by an Emmy Noether Fellowship GZ: UE188/2-1 from the Deutsche Forschungsgemeinschaft (DFG; to S.Ü.) and through the collaborative research council 1101 (SFB1101; to G.L.). We thank the confocal microscopy facility of ZMBP that is supported by funds from DFG (INST 37/819-1 FUGG and INST 37/965-1 FUGG) and the confocal microscopy facility of RUB (DFG Project number 523980288, GZ:INST 213/1180-1 FUGG). Macek Lab is supported by DFG funds (INST 37/1050-1 FUGG and INST 37/1255-1 FUGG).

794 ## Author Contribution

795 S.Ü. conceived the project. G.L. performed most experiments, analyzed the data, and performed
796 all computational analysis. M.R. performed the *in vitro* ubiquitination assays. D.B performed
797 the EMSA, assisted with the Luciferase reporter assay and the molecular cloning. D.S.
798 generated the *rpt2a-2 Pma* transcriptome under the supervision of F.B..M.F.W and B.M.
799 performed LC-MS/MS analysis. S.Ü. wrote the manuscript together with G.L..

800

801 ## Experimental model and Subject Details

802 ***Arabidopsis thaliana* lines and growth conditions**

803 *A. thaliana* Columbia-0 (Col-0) ecotype was considered as WT. T-DNA insertion mutants for
804 *NAC53* (*nac53-1*, SALK_009578C) and *NAC78* (*nac78-1*, SALK_025098) were obtained from
805 Richard Vierstra and previously described (Gladman et al., 2016). T-DNA insertion mutants for
806 *RPT2a* was previously described (Lee et al., 2011; Üstün et al., 2016). T-DNA insertion mutants
807 for *HRD1a (hrd1a*, SALK_032914) and *HRD1b* (*hrd1b,* SALK_061776) were obtained from
808 Yasin Dagdas and previously described (Su et al., 2011).
809 *promUBQ10*::GFP-NAC53 and *promUBQ10*::GFP-NAC78 transgenics lines were obtained by
810 *Agrobacetrium tumefaciens* floral dipping (Clough and Bent, 1998) of Col-0 plants. Positive
811 transformants were selected by BASTA spraying and seeds were harvested individually. The
812 following generations were sawed on ½ Murashige and Skoog (MS) media supplemented with
813 10µM phosphinotricin for segregation analysis. Two independent lines showing a 75% survival
814 rate for each construct were kept for subsequent experiments.
815 For experiments on seedlings, seeds were surface sterilized 10min with 1.3% sodium
816 hypochlorite. Seeds were then sown on ½ MS medium supplemented with 1% sucrose and
817 stratified for 2 days in cold room to synchronize germination. Plants were next grown under
818 long day conditions (light/dark cycles: 16h 22°C/8h 20°C, 130µmol.mm².s^{-1} light intensity,
819 70% relative humidity).
820 For experiments on adult plants, seeds were sown on soil soaked with water in individual pots.
821 Trays were put directly in the growth chamber under short day conditions (light/dark cycles:
822 12h 22°C/ 12h 20°C, 90µmol.mm².s^{-1} light intensity, 70% relative humidity). Seven days after
823 germination, excessive number of seedlings were removed from individual pots to obtain one
824 plant per pot. Plants were grown under same conditions until use (typically 21 to 28 more days).

825

826 ***Nicotiana benthamiana* growth**

827 *N. benthamiana* plants were grown under long day conditions (light/dark cycles: 16h/8h, at
828 21°C and 70% humidity) and typically used 4 weeks after germination for confocal microscopy
829 experiments and 5 weeks after germination for co-immunoprecipitation experiments.
830
831 **Bacterial strains**
832 *For Pseudomonas syringae* pv. *tomato* DC3000 wild-type and *Pseudomonas syringae* pv.
833 *maculicola* strains ES4326 were grown on King's B medium containing rifampicin 100µg.mL^{-}
834 ^{1} at 28°C. For floral dipping and transient expression in *Nicotiana benthamiana* leaves,
835 *Agrobacterium tumefaciens* C58C1 strain was grown in LB broth high salt (Duchefa L1704)
836 containing the required antibiotics at 28°C. For molecular cloning, *Escherichia coli* Top10
837 strain was grown in LB broth high salt (Duchefa L1704) containing the required antibiotics at
838 37°C. For protein purification, *Escherichia coli* BL21 (DE3) was grown in LB broth high salt
839 (Duchefa L1704) containing the required antibiotics at 37°C or 16°C.
840

841 ## Method Details

842 **Molecular cloning**
843 For chimeric protein constructs generated in this study, protein coding sequence (CDS) of the
844 desired genes were amplified from *A. thaliana* cDNA with addition of flanking region for
845 subsequent cloning process.
846 For Golden Gate based cloning (Binder et al., 2014), CDS were amplified with addition of
847 flanking regions including BpiI/BsaI sites (Fw: 5'-GAGAAGACGATACGGGTCTCACACC-
848 3'; Rv: 5'-GAGAAGACGACAGAGGTCTCACCTT-3'). PCR products were gel purified and
849 inserted into LI module (Binder et al., 2014) backbone using BpiI/T4 ligase (both Thermo
850 Scientic) cut-ligation procedure (40 cycles, 37°C 2min/16°C 5min). The resulting product was
851 transformed into *E. coli* Top10 followed by gentamycin selection. Positive clones were used for
852 plasmid miniprep (NEB) and verified by sanger sequencing. For generation of expression
853 constructs, the LI CDS module and desired other modules (e.g., promoter, tag, terminator etc.)
854 were assembled in the LIIa F 1-2 vector (Binder et al., 2014) using BpiI/T4 ligase (both Thermo
855 Scientic) cut-ligation procedure (40 cycles, 37°C 2min/16°C 5min). Resulting product was
856 transformed into *E. coli* Top10 followed by spectinomycin selection. Positive clones were
857 verified for correct assembly by colony PCR following by enzyme restriction analysis. The
858 obtained construct was then transformed into *A. tumefaciens* C58C1 for subsequent use.
859 For GATEWAY™ based cloning, CDS were amplified with addition of attb1/attb2 flanking
860 regions (attb1-fw 5'-GGGGACAAGTTTGTACAAAAAAGCAGGCTTC-3'; attb2-rv 5'-

861 GGGGACCACTTTGTACAAGAAAGCTGGGT-3'). PCR products were gel purified and
862 inserted into pDONR221 via BP clonase™ II enzymatic reaction. Alternatively, GATEWAY™
863 compatible entry clone was generated by performing a BsaI/T4 ligase cut-ligation from LI
864 module to pENTR-BsaI (Binder et al., 2014). Resulting product was transformed into *E. coli*
865 Top10 followed by kanamycin selection. Positive clones were used for plasmid miniprep (NEB)
866 and verified by sanger sequencing. For generation of expression constructs, pDONR/pENTR
867 clone was used for LR Clonase™ II enzymatic reaction into the desired destination vectors.
868 Resulting product was transformed into *E. coli* Top10 followed by spectinomycin or
869 carbenicillin selection. Positive clones were verified by colony PCR. The obtained construct
870 was then transformed into *A. tumefaciens* C58C1 or *E. coli* BL21 (DE) for subsequent use.
871
872 **Seedlings phenotyping**
873 For phenotyping assay, seeds were sown on ½ MS 1% sucrose round petri dish supplemented
874 with the indicated concentration of drug or a mock treatment.
875 After 10 to 14 days of growth fresh weight was measured. Seedlings were carefully extracted
876 from the media with a curved tweezer (Dumont Nr. 7) ensuring that the entire root was taken.
877 For one replicate, 5 representative seedlings were scaled together on an analytical scale
878 (resolution 0.0001g). Typically, 5 replicates were measured for subsequent statistical analyses.
879
880 **Transient expression in *N. benthamiana* leaves**
881 Bacterial suspension was centrifuged for 4min at 4000g after overnight incubation of *A.*
882 *tumefaciens* strain carrying the desired expression construct. Supernatant was removed and
883 pellet was resuspended in 500µl of agroinfiltration buffer (10mM $MgCl_2$, 10mM MES pH 5.7).
884 OD600 was measured and infiltration solutions were diluted to reach final 0.5 OD600 in
885 agroinfiltration buffer supplemented with 200µM acetoseryringone. Solutions were incubated
886 in dark at least 1h prior to infiltration. Infiltrated tissues were used 30h post infiltration for
887 subsequent experimental procedures.
888
889 **Protein purification**
890 Recombinant proteins were expressed in E. coli BL21(DE3) by IPTG induction. Bacterial
891 solution was centrifuged 20min at max speed and pellet was subjected to sonication after
892 resuspension in 1mL MBP-buffer (20 mM TRIS-HCl pH 7.5, 200mM NaC, 1mM EDTA) or
893 1mL IPP50 (10 mM Tris-HCl, pH 8.0. 150mM NaCl, 0.1% NP40). Sonicated samples were
894 used for purification by affinity chromatography using amylose resin (New England Biolabs)

895 for MBP-NAC53/78 or glutathione sepharose 4B (cytiva) for GST-HRD1a/b. For recombinant
896 His-UBA1 and His-UBC8 protein were purified using Ni-Ted resin (Macherey-Nagel).
897
898 ***In vitro* ubiquitination assay**
899 In vitro ubiquitination assay was performed as previously described (Leong et al., 2022).
900 Purified proteins were used for in vitro ubiquitination assays. Each reaction of 30 ml final
901 volume contained 25 mM Tris–HCl, pH 7.5, 5 mM MgCl2, 50 mM KCl, 2 mM ATP, 0.6 mM
902 DTT, 2 µg ubiquitin, 200 ng E1 His- AtUBA1, 1.2 µg E2 His-AtUBC8, 2 µg of GST-HRD1a/b,
903 and 0.3 µg of MBP-NAC53/78. Samples were incubated for 1 h at 30°C, and the reaction was
904 stopped by adding SDS loading buffer and incubated for 10 min at 68°C. Samples were
905 separated by SDS–PAGE electrophoresis using 4–15% Mini-PROTEAN® TGX™ Precast
906 Protein Gels (BioRad) followed by detection of the ubiquitinated substrate by immunoblotting
907 using anti-MBP (New England Biolabs), anti-GST and anti-ubiquitin (Santa Cruz
908 Biotechnology) antibodies.
909
910 **Co-immunoprecipitation**
911 Plant tissue was homogenized in a mortar with liquid nitrogen to keep the sample frozen during
912 the process. The powder was then transferred into a 50mL centrifuge tube and 1ml of extraction
913 buffer (10% glycerol, 25 mM Tris pH 7.5, 1 mM EDTA, 150 mM NaCl, 1 mM DTT, 0.5%
914 Triton X, 1X protease cocktail inhibitor (Sigma)) was added per gram of tissue. Obtained
915 sample were vortexed for 3min and incubated in cold room on rotator in cold room for 10min
916 following a 30min centrifugation at 4000g, 4°C. Supernatant was filtered through 3 layers of
917 miracloth (Merck 475855-1R) in a 15mL centrifuge tube. 50µl of filtrate was sampled as input
918 at this step, supplemented with 12.5µL laemmli buffer 4X (Biorad) and boiled for 10min at
919 90°C. Next, 10µl of ChromoTek GFP-Trap® or RFP-Trap Agarose beads per gram of tissue
920 were added and tubes were incubated 2-3h in cold room. Tubes were then centrifuge at 800g
921 for 1min; supernatant was carefully removed and pelleted beads were transferred to 1.5mL
922 microcentrifuge tube in 1mL of washing buffer (10% glycerol, 25 mM Tris pH 7.5, 1 mM
923 EDTA, 150 mM NaCl, 0.5% Triton X-100, 1X protease cocktail inhibitor (Sigma)). Washing
924 was perfomed by centrifugation at 800g for 1min using 1mL washing buffer. After last washing,
925 10µL of Laemmli buffer 2X (Biorad) was added to equal amounts of beads and sample was
926 boiled 10min at 90°C.
927
928 **RNA isolation & RT-qPCR**

929 Total RNA isolation was performed using RNeasy Plant Mini Kit (Qiagen 74904). All steps
930 were performed according to manufacturer instructions. To exclude potential contaminant
931 DNA, RNA samples were subjected to DNase I treatment (Thermo scientific™) following
932 provider instructions. For RNA sequencing, integrity and RNA concentration was determined
933 (2100 Bioanalyzer, Agilent). For RT-qPCR sample analysis was adapted from Langin and Üstün
934 (2023); cDNA synthesis was performed using LunaScript® RT SuperMix Kit (NEB) following
935 provider recommendation. qPCR was performed using MESA BLUE qPCR 2X MasterMix
936 Plus for SYBR® Assay (Eurogentec) using a 2-step reaction protocol for 40cycles with
937 systematic evaluation of primer melting curve. mRNA level was quantified based on the ΔΔCt
938 method followed by Log2 transformation.
939
940 **NanoLC-MS/MS analysis and data processing**
941 For purification, proteins were subjected to a NuPAGE 12% gel (Invitrogen) and in-gel trypsin
942 digestion was done on Coomassie-stained gel pieces, as described previously (Borchert et al,
943 2010) with a modification: iodoacetamide was used instead of chloroacetamide for
944 carbamidomethylation of cysteine residues to avoid formation of lysine modifications isobaric
945 to two glycine residues left on ubiquitinylated lysine after tryptic digestion. Next, peptides
946 mixture were desalted using C18 Stage tips and run on an Easy-nLC 1200 system coupled to a
947 Q Exactive HF-X mass spectrometer (both Thermo Fisher Scientific) as described elsewhere
948 (Kliza et al., 2017) with some modifications: separation of the peptide mixtures was done using
949 a 87-min segmented gradient from 10-33-50-90% of HPLC solvent B (80% acetonitrile in 0.1%
950 formic acid) in HPLC solvent A (0.1% formic acid) at a flow rate of 200 nl/min. The seven most
951 intense precursor ions were sequentially fragmented in each scan cycle using higher energy
952 collisional dissociation (HCD) fragmentation. In all measurements, sequenced precursor
953 masses were excluded from further selection for 30 s. The target values were 105 charges for
954 MS/MS fragmentation and 3 × 106 charges for the MS scan.
955 Acquired MS spectra were processed with MaxQuant software package version 1.5.2.8 with an
956 integrated Andromeda search engine. For *in vivo* IP samples, database search was performed
957 against a *N. benthamiana* database containing 74,802 protein entries (Kourelis et al., 2019), the
958 sequences of eGFP-NAC53/78, mCerrulean3-NAC53/78-mCherry and 285 commonly
959 observed contaminants.
960 For *in vitro* ubiquitination samples, database search was performed against the Uniprot *E. coli*
961 database, the sequences of MBP-NAC53/78, GST-HRD1a/b and 285 commonly observed
962 contaminants.

963 Endoprotease trypsin was defined as a protease with a maximum of two missed cleavages.
964 Oxidation of methionine, phosphorylation of serine, threonine, and tyrosine, GlyGly dipeptide
965 on lysine residues, and N-terminal acetylation were specified as variable modifications.
966 Carbamidomethylation on cysteine was set as a fixed modification. Initial maximum allowed
967 mass tolerance was set to 4.5 parts per million (ppm) for precursor ions and 20 ppm for fragment
968 ions. Peptide, protein, and modification site identifications were reported at a false discovery
969 rate (FDR) of 0.01, estimated by the target-decoy approach (Elias and Gygi). The iBAQ
970 (Intensity Based Absolute Quantification) and LFQ (Label-Free Quantification) algorithms
971 were enabled, as was the "match between runs" option (Schwanhäusser et al., 2011).
972
973 **Photosynthesis monitoring**
974 For photosynthetic pigment concentration, 2 leaf discs (6mm) were sampled in a 2mL
975 microcentrifuge tube after the indicated treatments and incubated over-night in 1mL acetone
976 100% on a rotating wheel in cold room. Tubes were next centrifuged for 3min at 400g. 200µl
977 of was then pipetted in a transparent 96-well plate and absorbance was measured at 470nm,
978 646nm and 663nm using a plate reader (Tecan Infinite 200 PRO®). Acetone 100% was used as
979 blank. Concentration was calculated as following:
980 Total Chlorophylls ($\mu g.ml^{-1}$): $((12.25*A_{662}) - (2.79*A_{646}) + (21.5*A_{646}) - (5.1*A_{663}))/0.2$
981 Total Carotenoids ($\mu g.ml^{-1}$): $((1000*A470-1.63*((12.25*A_{662}) - (2.79*A_{646})) -$
982 $85.02*((21.5*A_{646}) -(5.1*A_{663})))/221)/0.2$
983 The equations for concentration calculation and procedure were obtained from Karlsruher
984 Institut für Technologie (KIT, https://www.jkip.kit.edu/molbio/998.php, "Chlorophyll and
985 Carotenoid determination in leaves") as an updated version of the original procedure
986 (Lichtenthaler, 1987).
987 Values were then then expressed as $ng.mm^2$ by dividing them by the total leaf area used for
988 extraction (typically $56.55mm^2$).
989 For photosynthetic efficiency, photosystem II (PSII) activity was measured by quantifying the
990 maximum photosystem II yield, Fv/Fm via the saturation pulse methods on dark acclimated
991 plants (Schreiber, 2004). After treatments, plants were acclimated in dark for 15min. Next,
992 leaves were detached and PSII activity was assessed by Fv/Fm values using the Imaging-PAM
993 chlorophyll fluorometers: Maxi version v2-46i, for measurements related to Figure 5 and Dual-
994 PAM100, for measurements related to Figure 6 (Walz GmbH, Effeltrich, Germany).
995
996 **Bacterial Infection**

997 For bacterial infections, *Pst* overnight liquid culture was centrifuged for 15min at 4000g.
998 Bacterial pellet was resuspended in 5mL of $MgCl_2$ 10mM prior to OD600 measurement.
999 For qPCR, RNAseq and western blot analysis; a *Pst* solution at OD600=0.2 was used. Adult
1000 plant leaves were infiltrated with a 1mL syringe (Braun) with the *Pst* infiltration solution or a
1001 control solution (10mM $MgCl_2$) and put back in growth chamber for 24h until sampling or
1002 further analysis.
1003 For IP and Chromatin-IP on *A. thaliana*, *Pst* infiltration was prepared as explained above and
1004 detached whole rosettes of adult plants were vacuum infiltrated 2 times 2 min at < 15mbar. For
1005 mock, control solution (10mM $MgCl_2$) was used similarly. Rosettes were put back in the growth
1006 chamber for 8h on multiple layers of wet tissue.
1007 For assessment of bacterial density (related to Figure 1C and 6D); *Pst* infiltration solution was
1008 prepared in 10mM $MgCl_2$ at an OD600 of 0.0001. Adult plant leaves were infiltrated with a
1009 1mL syringe (Braun) with the *Pst* infiltration solution and put back in growth chamber for 72h
1010 in high humidity conditions. After 3 days, 2 leaf disks per replicates were sampled with a biopsy
1011 punch 6.0mm (Harris Uni-Core) in a 1.5mL microcentrifuge tube. Tissue was homogenized in
1012 200µl 10mM and a serial dilution of factor 10 was done for each replicate in 200µL nano pure
1013 water until 10^{-6} dilution was reached. For bacterial counting, 20µL of several resulting dilutions
1014 (typically 10^{-5} and 10^{-6}) were plated on KB media with rifampicin for each replicate. Growing
1015 colony-forming units were counted and Log10CFU/cm² was calculated for graphical
1016 representation and statistical testing.
1017
1018 **Chromatin Immuno-Precipitation**
1019 For Chromatin-IP, after Arabidopsis rosettes were vacuum infiltrated for 30min with a fixation
1020 buffer solution (1% formaldehyde, 10mM KH2PO4 pH 7, 50mM NaCl, 0.1M sucrose, 0.01%
1021 Triton X-100) to cross-link protein-DNA. Plant material (typically 1g) was dried and frozen in
1022 liquid nitrogen for each replicate. Tissue was next ground in 5mL nuclei isolation buffer (20mM
1023 Hepes pH8, 250mM sucrose, 1 mM $MgCl_2$, 5mM KCl, 40% Glycerol, 0.25% Triton X-100,
1024 0.1mM PMSF, 0.1% 2-mercaptoethanol, 1µM BTZ). The resulting solution was filtered
1025 through three layers of miracloth paper in a 50mL centrifuge tube following 10min
1026 centrifugation at 4°C, 3000g. Pellet was resuspended in 1mL nuclei isolation buffer and
1027 transferred into a 1.5mL microcentrifuge tube. Tube was centrifuged 5min, at 4°C, 3000g and
1028 the previous step was repeated once. Pellet was resuspended in 200µl M3 buffer (10mM
1029 KH2PO4 pH7, 0.1mM NaCl, 10mM 2-mercaptoethanol) and recentrifuged 5min, 4°C, 3000g.
1030 Nuclei pellet was resuspended in 1mL sonication buffer (10mM KH2PO4 pH7, 0.1mM NaCl,

1031 0.5% Sarkosyl, 10mM EDTA). Sonication was performed with an Active Motif Sonicator (Amp
1032 25%; Pulse: 30sec ON – 30sec OFF; Timer: 300sec). Sonicated sample was centrifuged for
1033 5min, 4°C at max speed. Supernatant was tranferred to a new 1.5mL microcentrifuge tube and
1034 10% (v/v) Triton X-100 was added to neutralize the sarkosyl. 5% (v/v) of this solution was
1035 saved in another 1.5mL microcentrifuge as input sample. For IP, 15µL ChromoTek GFP-Trap®
1036 were activates in 15µL IP buffer (50mM Hepes pH 7.5, 150mM NaCl, 5mM $MgCl_2$, 10uM
1037 ZnSO4, 1% Triton X -100, 0.05% SDS) and added to the tube and incubated for 3h on a rotating
1038 wheel at 4°C. Beads were washed for 4 rounds by centrifuging for 30sec, at 1000g and
1039 subsequent incubation on rotating wheel in 500µL buffer for 3 min; twice in IP buffer, once in
1040 LNDET buffer (0.25 LiCl, 1% NP-40, 1% deoxycholate, 1mM EDTA pH 8, 10mM Tris pH 8)
1041 and once in TE buffer (10mM Tris pH 8, 1mM EDTA pH 8). After the last washing step, beads
1042 were centrifuged for 30sec at 1000g, resuspended in 200µL EB buffer (50mM Tris pH 8, 10mM
1043 EDTA pH 8, 1% SDS) supplemented with 8µL 5M NaCl to reverse cross-linking and incubated
1044 at 65°C for at least 6h. At this step input sample was added and treated similarly. For protein
1045 digestion, 1µL of Proteinase K (Thermo Scientific) was added and incubated for 1h at 45°C.
1046 Next, DNA was purified using a PCR purification kit (NEB) following manufacturer
1047 instructions.
1048 For DNA quantification, qPCR was performed using MESA BLUE qPCR 2X MasterMix Plus
1049 for SYBR® Assay (Eurogentec) using a 2-step reaction protocol for 40 cycles and each sample
1050 was processed in technical triplicates. For quantification, % of input was calculated and used
1051 for graphical representation and statistical analysis.
1052
1053 **Immunoblot analysis**
1054 For immunoblot analysis, sample processing was adapted from (Langin and Üstün, 2023); 2
1055 leaf discs from *N. benthamiana* or *A. thaliana* were sampled using a biopsy punch 6mm (Harris
1056 Uni-Core) in 2mL microcentrifuge tube containing 2 glass beads (2mm) for one replicate in the
1057 given condition and frozen in liquid nitrogen. Tissue was homogenized using a Tissue Lyzer II
1058 (Qiagen), 2 times 30sec, frequency: 25; followed by the addition of 150µL protein extraction
1059 buffer (100mM Tris-HCl pH 7.5, 3% SDS, 10mM EDTA) per tube. Tubes were next mixed
1060 with the Tissue Lyzer II, 2 times 15sec, frequency: 15. Finally, 50µL laemmli buffer 4X (biorad)
1061 was added and samples were boiled for 10min at 95°C. Tubes were centrifuged for 1min at
1062 13000g and 150µL of the supernatant was transferred in a new 1.5mL microcentrifuge tube and
1063 kept at -20°C until use.

1064 Western blotting was done by SDS-PAGE using TGX FastCast 10% Acrylamide gels (Biorad)
1065 with 1.0 mm spacer plates according to manufacturer recommendations. SDS-PAGE was
1066 performed in TGS running buffer (25 mM Tris pH 8.3, 192mM glycine, 0.1% SDS) and proteins
1067 were transferred on PVDF membrane 0.2mm (Biorad) using Trans-Blot Turbo system (Biorad)
1068 according to manufacturer recommendations. PVDF membranes were incubated for 1h in
1069 TBST (50mM Tris-HCl pH 7.5, 150mM NaCl, 0.1% Tween20) solution containing 5%
1070 Skimmed-Milk followerd by antibody incubation in TBST 5% Milk for 1h at RT or over-night
1071 at 4°C. Membranes were washed 3 times in TBST for 5min and 1 time in TBS for 5min. HRP
1072 chemiluminescence was detected using Amersham™ ECL Select™ detection reagent and
1073 images were taken using a CCD camera.
1074
1075 **Electromobility Shift Assay**
1076 For EMSA assays, complementary DNA oligos were synthesized by EuroFins Genomics with
1077 ATTO565 dye linked to the 5' end of minus strand for probes. To generate double stranded
1078 probes, complementary oligos were incubated at 2µM in annealing buffer (25mM HEPES-
1079 KOH pH 7.8, 40mM KCl) at 70°C for 5min and cool down to room temperature.
1080 EMSA reactions were performed in 20µL reaction buffer (25 mM HEPES-KOH pH 7.8, 40
1081 mM KCl, 1 mM DTT, 10% Glycerol) using 1µg purified MBP-NAC53/78 and 50ng DNA probe
1082 for 30min at 25°C. Reactions were subjected to native polyacrylamide migration with TGX
1083 FastCast 7.5% Acrylamide gels (Biorad) in TAE (Tris-base 40 mM pH 8.3, 20mM acetic acid,
1084 1mM EDTA). After migration, probes were imaged using a Typhoon FLA 9000 Gel Scanner.
1085
1086 **Luciferase reporter assay in Protoplasts**
1087 For promoter activity analysis, *Arabidopsis* mesophyll protoplasts were generated adapted from
1088 Yoo et al., 2007. Leaves from adult plants were cut into strips (0.5mm) and incubated in the
1089 Maceroenzyme R-10 (Duchefa M8002) and Cellulase Onozuka R-10 (Duchefa C8001) solution
1090 for 3h. Solution was subsequently filtered through 3 layers of miracloth paper (Merck 475855-
1091 1R) in a 50mL centrifuge tube. Protoplast suspension was centrifuged for 1min at 200g at 4°C
1092 and supernatant was carefully removed from the protoplast pellet. Pellet was washed twice with
1093 W5 buffer (Yoo et al., 2007) in ice. Protoplasts were resuspended in MMG buffer (Yoo et al.,
1094 2007), 200µL dispatched in 2mL microcentrifuge tube and 5µg of each plasmid were
1095 transfected by addition of 220µL 30% PEG4000 (Sigma-Aldrich 81240) solution for 15min.
1096 880µL of W5 was added to stop the reaction followed by 1min centrifugation at 200g.
1097 Supernatant was removed and transfected protoplast pellet were resuspended in 250µL WI

1098 buffer (Yoo et al., 2007). Tubes were left over night in dark for construct expression prior to
1099 measurements.
1100 Luciferase quantification was performed according to Dual-Luciferase® Reporter Assay
1101 System from Promega recommendation (see link). Protoplast expressing the desired contructs
1102 were centrifuged for 15sec at max speed. Supernatant was removed and protoplast pellet was
1103 resuspended in 100µl of 1X passive lysis buffer (see link). The lysed protoplast suspension was
1104 transferred into a white 96-well plate (Thermo Scientific™ Nunc™ MicroWell™).
1105 Measurement of Firefly Luciferase (FfLuc, reporter constructs) was performed by adding 40µl
1106 LARII reagent (see link) and luminescence was measured using a plate reader (Berthold Tristar
1107 LB 940). Measurement of Renilla Luciferase (RnLuc, internal control) was performed adding
1108 40µl of Stop & Glo® (see link) and luminescence was measured. Due to an apparent cross-talk
1109 between NAC53/78ΔTM expression and the *prom35S*::*RnLuc* constructs (see AtNAM DBD
1110 and 35S promoter interaction, (Duval et al., 2002); the results showed Figure S5 are based on
1111 the FfLuc luminescence only.
1112

1113 ## QUANTIFICATION AND STATISTICAL ANALYSIS

1114 For all statistical analysis, R programming language was used in the Rstudio environment.
1115 For non-omics data, the statistical test and associated p value threshold for each analysis are
1116 indicated in the figure legends. Data dispersion, medians and quantiles are represented with
1117 boxplots and replicates displayed in every figures. For bar plots in Figure S2, number of
1118 replicates are indicated in the figure legend, error bars represent the standard deviation from the
1119 mean.
1120

1121 **RNA sequencing**

1122 For *rpt2a-2 Pma* transcriptome, sequencing was performed by ATLAS Biolabs, Berlin. For
1123 *nac53-1 78-1 Pst* transcriptome, sequencing was performed by the NGS Competence Center,
1124 Tübingen. After quality control, reads were mapped to the *A. thaliana* TAIR10 reference
1125 genome. The mapped reads were counted with *htseq-count* for subsequent analysis. Log2FC
1126 and false discovery rate (FDR) were determined using R package DEseq2 (Love et al., 2014)
1127 with default settings. A gene is considered significantly differentially expressed when its FDR
1128 < 0.05. Log2FC threshold is indicated in the figure legends according to the analysis.
1129

1130 **IP-MS/MS analysis**

1131 For IP-MS/MS analysis in Figure 2 and Figure S2, Log2FC and false discovery rate (FDR) for
1132 each protein group were determined using R package IPinquiry4 (Kuhn et al., 2023). For GFP-
1133 NAC53/78 mock conditions, free-GFP mock was used as control; for GFP-NAC53/78 *Pst*
1134 conditions, free-GFP *Pst* was used as control; for CFP-NAC53/78-RFP N-ter conditions, free-
1135 GFP was used as control; for CFP-NAC53/78-RFP C-ter conditions, mCherry-HDEL was used
1136 as control. For downstream analysis, to each protein group a unique Agi-code was assigned by
1137 blasting every *N. benthamiana* protein present in the protein group and taking the most frequent
1138 Agi-code with the best E-value. An e-value threshold of e-10 was used, in case of absence of
1139 *A. thaliana* the protein group was not considered for downstream analysis. For heatmap
1140 representation in Figure S1H-K, in case multiple protein groups correspond to the same *A.*
1141 *thaliana* orthologs the mean Log2FC is represented.
1142
1143 **Meta-Transcriptomic analysis**
1144 For meta-transcriptomic analysis in Figure 6 and FigureS6, fragments per kilobase per million
1145 counts were retrieved from the data base (http://ipf.sustech.edu.cn/pub/athrna/). Log2FC for
1146 individual genes in every project was calculated based on the control RNAseq libraries as
1147 annotated in the original publication (Zhang et al., 2020). Filtering of relevant projects for
1148 subsequent correlation analysis was done based on the median |Log2FC|. Median|Log2FC| >
1149 0.5 was used for identification of projects with at least one gene cluster transcriptionally
1150 impacted (see Table S3, related to Figure 6H) and median |Log2FC| > 0.3219 was used for
1151 identification of projects in which 26S proteasome and PhANGs clusters were co-
1152 transcriptionally impacted (see Table S3, related to Figure S6G). Pearson correlations were
1153 calculated using base R function. Only correlations with p-value < 0.05 were considered
1154 significant and used for calculation of mean/median.
1155
1156 **Omics downstream analysis: Gene ontology, Protein Network, subcellular enrichment &**
1157 **cis-element analysis**
1158 For Gene Ontology enrichment, the list of Agi-code was uploaded into ShinyGO software
1159 (http://bioinformatics.sdstate.edu/go/, (Ge et al., 2020). Cladogram of the indicated number of
1160 top terms for the indicated type of terms was used for graphical representation. Table of
1161 annotations was extracted for further analysis.
1162 For network creation, list of Agi-code was provided to the string database (https://string-
1163 db.org/). Table of interactions was extracted and uploaded to cytoscape software
1164 (https://cytoscape.org/) for network generation, design, and annotation. For purposes of clarity,

1165 network nodes were manually arranged. Edge transparency relate to the strength of interaction
1166 with opaque edges corresponding to strong interactions and transparent edges to weak
1167 interactions. Node color corresponds to manual annotation inferred based on GO annotations
1168 and further curated from the literature.
1169 For subcellular compartment enrichment, the list of Agi-code was uploaded into SUBA5db
1170 (https://suba.live/). Compartment annotation was extracted, and occurrence of every
1171 compartment was counted to estimate the list distribution. For theorical distribution 20 Agi-
1172 code lists of the same length were randomly generated and processed similarly. The mean
1173 distribution of the 20 lists was used as theorical distribution. Enrichment for every compartment
1174 was calculated as a Log2FC of the ratio between the observed proportion and the theorical one.
1175

1176 **Cis-Regulatory Element analysis**

1177 For cis-regulatory element analysis, promoter sequences of 1000bp upstream of the
1178 transcription starting site were retrieved from plant ensembl database using biomart browser
1179 (https://plants.ensembl.org/biomart/). For identification of novel cis-regulatory elements in
1180 Figure 5A, promoter sequences of the several gene clusters were analyzed using the STREME
1181 software (https://meme-suite.org/meme/tools/streme) with default settings. For mapping and
1182 counting in Figure S5B and S5C, promoter sequences were analyzed in R using regular
1183 expression matching for "tgggc" or "gccca" pattern.
1184

1185 **Immunoblot semi-quantitative analysis**

1186 Quantification of protein abundance based on immunoblot signals (related to Figure 4D and
1187 5G) was adapted from (Gallo-Oller et al., 2018). Raw image of the immublot signals against
1188 the protein of interest and the corresponding loading control were processed using Fiji software
1189 (https://imagej.net/software/fiji/downloads). Image was converted to 8-bit format. A duplicated
1190 image was used to generate a background image using the function "Substract Background"
1191 with a ball radius value of 50 pixels and the option "create background (don't substract)
1192 activated. The resulting background was then subtracted from the original 8-bit image with the
1193 function "Image Calculator". Individual lanes were quantified by measurement of the peak area
1194 after circumscription with the rectangular ROI selection and "Gels" function. The obtained
1195 values for individual bands were normalized by the corresponding loading control values. For
1196 calculation of Log2FC in abundance, quantification of bands in infected sample were divided
1197 by the corresponding mock sample quantification of the same genotype; the obtained ratio was
1198 next transformed using Log2 function.

1199

1200 **Confocal microscopy imaging**

1201 Confocal microscopy was done using an inverted Zeiss LSM 880 microscope, an upright Leica
1202 SP8 microscope or an inverted Leica Stellaris 8 microscope. For mCerrulean3 imaging,
1203 excitation was done using a 458nm laser and emission signal was measured from 465nm to
1204 500nm; for eGFP or sGFP imaging, excitation was done using a 488nm laser and emission
1205 signal was measured from 510nm to 540nm; for mRFP or mCherry imaging, excitation was
1206 done using a 561nm laser and emission signal was measured from 590nm to 630nm; in addition
1207 chlorophyll auto fluorescence was measured in the far red wavelength (> 700nm). Images were
1208 acquired with a 40X water immersion objective, pinhole was set to 1 airy unit, resolution of
1209 acquisition was set to at least to 1024x1024 with a line average of 4.

1210 After acquisition images were processed in Fiji Software. For images obtained from Leica
1211 microsystem devices, a gaussian blur (radius 0.75) was applied for a smoother rendering. For
1212 clarity purposes, contrast on the individual channels was manually adjusted.

1213 For subcellular quantification of GFP signal (related to Figure S3), all images used were
1214 acquired on the Zeiss LSM 880 with a 16bits depth. Prior to imaging seedlings were incubated
1215 for 10min in a 10µM propidium iodide (PI) ½ MS solution followed by a brief washing in clear
1216 ½ MS. PI fluorescence was excited with the 488nm laser and measured from 590nm to 660nm.
1217 For all acquisitions within an experimental repetition the laser power and gain for the GFP
1218 channel was kept constant. For segmentation, images were processed in Fiji Software. Each
1219 cell was segmented using the polygon ROI selection tool. Each nucleus was segmented in the
1220 same order using the oval ROI selection tool. Next, mean intensity and integrated density of
1221 the whole cell, the nucleus, and the whole cell after removal of nucleus ROI (considered as
1222 cytosolic ROI) was measured. Signal proportion in the nucleus was quantified by the ratio
1223 between integrated density of nucleus ROI by whole cell ROI and ratio of signal between
1224 nucleus and cytosol was calculated by the ratio between nucleus ROI mean intensity and
1225 cytosolic ROI mean intensity.

1226 For calculation of co-localization index in Figure 2C, the image J plugin "co-localization
1227 finder" was used and calculated pearson index is provided in the Figure. For calculation in
1228 Figure 3C, plot profile of GFP and RFP signals was extracted at the indicated line using Fiji
1229 software and the pearson index indicated on the Figure was calculated between the two profile
1230 values on R.

1231

1232 **RESOURCE AVALAIBILITY**

1233 Source code of R and Python3 scripts used for the several computational analysis done in this
1234 study will be put available on https://github.com/Gogz31 or can be directly requested.
1235

1236 ## DATA AVAILABILITY

1237 The mass spectrometry data from this publication will be made available on the PRIDE archive
1238 (https://www.ebi.ac.uk/pride/archive/) and with the identifier (PXDXXXXX; and
1239 (PXDXXXX). All relevant proteomics data are made available in the supplemental information.
1240

1241 ## SUPPORTING INFORMATION

1242 **Figure S1.** Deciphering the details of NAC53/78 interactome. Related to Figure 2.
1243 **Figure S2.** NAC53/78 are subjected to high level of poly-ubiquitination. Related to Figure 3.
1244 **Figure S3.** NAC53/78 association with CDC48 is required for their nuclear translocation.
1245 Related to Figure 3.
1246 **Figure S4.** Transcriptional analysis of proteotoxic stress reveals a trade-off between 26S
1247 proteasome and other biological process. Related to Figure 4.
1248 **Figure S5.** Characterization of the NAC53/78-PRCE module in PhANGs promoters. Related
1249 to Figure 5.
1250 **Figure S6.** The proteasome autoregulatory feedback loop transcriptional signature is a systemic
1251 response to environmental cues. Related to Figure 6.
1252 **Table S1.** Spectral count enrichment of the protein groups identified in NAC53/78 common
1253 interactome. Related to Figure 2.
1254 **Table S2.** Enrichment of mRNA of 538 DEGs in *nac53-1 78-1* Pst, overlapping with *rpt2a-2*
1255 Pma and/or MG132 24h data sets. Related to Figure 4.
1256 **Table S3.** List of the several RNAseq projects identified in study in which 26S proteasome
1257 and/or PhANGs are differentially regulated. Related to Figure 6.
1258

1259 ## FIGURE LEGENDS

1260 **Figure 1. NAC53/78 are central integrators of various proteotoxic stress conditions.**
1261 (A) The role of the 26S Proteasome in degradation of proteins from distinct subcellular
1262 compartments. Prime site of action of the several treatments used in this study: Blunt head
1263 arrows indicate enzymatic activity suppression; pointed head arrows indicate trigger of
1264 substrate accumulation.
1265 (B) Fresh weight of seedlings grown under the indicated treatments at 10-14 day after
1266 germination (dag). Fresh weight is expressed as a percentage of Col-0 mock conditions.
1267 Boxplots colors refer to the genotype. Statistical significance is assessed by a Wilcoxon-Mann-
1268 Whitney test (p values: n.s. > 0.05; * < 0.05; ** < 0.01). Every treatment has been repeated at
1269 least twice with similar results.
1270 (C) Bacterial density in Log10 Colony-Forming-Unit (CFU) per leaf cm^2. Statistical
1271 significance is assessed by a Wilcoxon-Mann-Whitney test (p values: n.s. > 0.05; ** < 0.01).
1272 Boxplots colors refer to the genotype as in panel B. The treatment has been repeated three times
1273 with consistent results.
1274 (B-C) Representative phenotypic pictures of Col-0 and *nac53-1 78-1* plants under several
1275 treatments are included.
1276 **Figure 2. NAC53/78 are part of an autoregulatory proteasome feedback loop.**

1277 (A) Confocal microscopy pictures of roots of GFP-NAC53/78 *Arabidopsis thaliana* transgenics
1278 at 7dag exposed to mock or BTZ 10µM treatment for 3h. Treatments were repeated at least
1279 three times with similar observations.
1280 (B) Immunoblot analysis against GFP on crude extract of seedlings related to panel A. Ponceau
1281 staining is used as loading control.
1282 (C) Confocal microscopy pictures of transiently co-expressed sTag-NAC53/78 with
1283 prom35S::RFP-HDEL or together in *N. benthamiana* epidermis cells. Pearson index (ρ)
1284 represents co-localization index. Scale bars = 10µm
1285 (D) Confocal microscopy pictures of transiently co-expressed sTag-NAC53/78 together or
1286 dTag-NAC53/78 alone in *N. benthamiana* epidermis cells. Scale bars = 10µm
1287 (E) Bar plots representing the number of significantly enriched proteins in the 4 IP-MS/MS
1288 conditions for NAC53 only, NAC78 only and NAC53+NAC78 (Common).
1289 (F) Cladogram of top 30 gene ontology (GO) terms for biological process (BP) enriched in the
1290 list of *A. thaliana* ortholog proteins found from NAC53/78 common interactome.
1291 (G) Protein network of the interacting candidates related to the GO BP terms annotated as
1292 "Transport" and "Proteolysis" in panel F.
1293 **Figure S1. Deciphering the details of NAC53/78 interactome. Related to Figure 2**
1294 (A) Chimeric NAC53/78 constructs generated in this study. Upstream promoter, fluorescent tag
1295 and protein domain of interests are represented.
1296 (B) Immunoblot against GFP on crude extracts of *N. benthamiana* leaves transiently expressing
1297 sTag-NACs in addition to mock or 6h BTZ (10µM) treatment. Ponceau staining is used as
1298 loading control.
1299 (C) Immunoblot against GFP or RFP on crude extracts of *N. benthamiana* leaves transiently
1300 expressing dTag-NACs in addition to mock or BTZ 10µM for 6h. Ponceau staining is used as
1301 loading control.
1302 (D) Immunoblot against GFP after immunoprecipitation (IP) with anti-GFP agarose beads on
1303 *N. benthamiana* leaf extracts transiently expressing sTag-NACs after mock or *PstΔHopQ*
1304 infection for 8h. The same samples were used for subsequent MS/MS analysis.
1305 (E) Immunoblot against GFP or RFP after IP with anti-GFP or anti-RFP agarose beads on *N.*
1306 *benthamiana* leaf extracts transiently expressing dTag-NACs. The same samples were used for
1307 subsequent MS/MS analysis.
1308 (F) Cladogram of top 30 GO terms for cellular components enriched in the list of *A. thaliana*
1309 ortholog proteins found in NAC53/78 common interactome.
1310 (G) Subcellular compartments enrichment in the list of *A. thaliana* proteins from NAC53/78
1311 common interactome based on their SUBA5db annotation. Statistical significance is provided
1312 through a chi-square testing.
1313 (H-K) Heatmap representing the peptide enrichment (Log2FC) of the protein clusters from the
1314 network Figure 2G.
1315 **Figure 3. ER-Anchored Protein Sorting (ERAPS) coordinates the subcellular fate of**
1316 **NAC53 & NAC78.**
1317 (A) Confocal microscopy pictures of GFP-NAC53/78 expressing *A. thaliana* roots. 7 dag
1318 seedlings were exposed to mock treatment, BTZ 10µM, CB-5083 10µM or LS-102 100µM for
1319 3h. The treatments were repeated at least three times with similar observations. Scale bars =
1320 10µm
1321 (B) Immunoblot against GFP on crude extracts of GFP-NAC53/78 *A. thaliana* adult plants
1322 infiltrated with mock treatment, BTZ 10µM, CB-5083 10µM or LS-102 100µM for 6h. Ponceau
1323 staining is used as loading control.
1324 (C) Confocal microscopy pictures of *N. benthamiana* transiently co-expressing GFP-
1325 NAC53/78 full-length (FL) or deleted for the transmembrane domain (ΔTM) with RFP-HRD1a
1326 or RFP-HRD1b. Pearson index (ρ) indicates correlation index at the orange lines.

1327 (D) Co-IP of RFP-HRD1a/b with GFP-NAC53/78. IP was performed with anti-GFP beads.
1328 GFP-HDEL and free-GFP were used as negative control. The experiment was repeated twice
1329 with similar results.
1330 (E) Immunoblot against GFP on crude extract of *N. benthamiana* leaves transiently expressing
1331 GFP-NAC53/78FL or ΔTM. Ponceau was used as loading control. Boxplots represent the
1332 relative ΔTM abundance compared FL.
1333 (F) *In vitro* trans-ubiquitination assays of GST-HRD1a/b against MBP-NAC53/78. Removal of
1334 E1 and ATP from the reaction was used as negative control. The experiment was repeated twice
1335 with similar results.
1336 (G) Representation of the ER-Anchored Protein Sorting (ERAPS) mechanism. NAC53/78 are
1337 ER-anchored proteins recognized and ubiquitinated by the HRD1 complex. The CDC48
1338 complex subsequently extracts NAC53/78 from the ER to mediate ER-Associated Degradation
1339 or allowing nuclear translocation in the context of proteasomal stress to mitigate proteotoxicity.
1340 **Figure S2. NAC53/78 are subjected to high level of poly-ubiquitination. Related to Figure**
1341 **3.**
1342 (A) *In vitro* analysis of LS-102 effect on HRD1a/b ubiquitination activity. Removal of E1 and
1343 ATP from the reaction was used as negative control.
1344 (B) Quantification of the inhibitory effect of LS-102 (100µM) on HRD1 activity. Bar plots
1345 represent the mean of three independent replicates with error bars representing the standard
1346 deviation.
1347 (C) Heatmaps representing the mean Log10 intensity of peptides bearing a di-glycine mark on
1348 the indicated lysin residue identified by MS/MS analysis of *in vitro* trans-ubiquitination
1349 reactions (see Figure 3F).
1350 (D) Heatmaps representing the mean Log10 intensity of peptides bearing a di-glycine mark on
1351 the indicated lysin residue identified by MS/MS analysis of IP samples generated for Figure 2.
1352 (E) Alignments of NAC53 and NAC78 peptide sequence regions around the identified lysin
1353 residues in panel C and D. Colors represent the residue conservation (green: conserved, shade
1354 of red: not conserved). All the identified lysins in one protein are conserved in the other.
1355 Underlined residues correspond to the mutated residues generated for the panel H and I.
1356 (F) *In vitro* trans-ubiquitination assays of GST-HRD1a/b against MBP-NAC53/78 in the
1357 presence of LS-102 inhibitor. Removal of E1 and ATP from the reaction was used as negative
1358 control.
1359 (G) Immunoblot analysis of *N. benthamiana* transiently expressing free-GFP, RFP-HDEL or
1360 dTag-NAC53/78 subjected to IP with anti-ubiquitin beads. The experiment was repeated twice
1361 with similar results.
1362 (H) Immunoblot analysis of *N. benthamiana* transiently expressing GFP-NAC53/78 mutated
1363 for 5 lysins (Mut., see panel E) or not (WT) subjected to IP with anti- ubiquitin beads.
1364 (I) Quantification of the relative ubiquitination levels assessed by the ratio between GFP signal
1365 and ubiquitin signal after IP as in panel H. Barplots represent the mean ratio of two replicates,
1366 normalized to the ratio of WT constructs with error bars representing the standard deviation.
1367 **Figure S3. NAC53/78 association with CDC48 is required for their nuclear translocation.**
1368 **Related to Figure 3.**
1369 (A) Confocal microscopy pictures of transgenic GFP-NAC53/78 root seedlings exposed to BTZ
1370 10µM, BTZ 20µM, CB-5083 10µM or CB-5083 20µM for 3h. Scale bars = 10µm
1371 (B) Confocal microscopy pictures of *N. benthamiana* leaves transiently co-expressing
1372 AtCDC48c-GFP with RFP-NAC53/78. Co-localization is visible in aggregate-like structures.
1373 Scale bars = 1µm
1374 (C) Confocal microscopy representative pictures (used for panel D-E) of transgenic GFP-
1375 NAC53/78 roots treated with BTZ 10µM and CB-5083 10µM followed by Propidium Iodide
1376 staining. Scale bars = 10µm

(D-F) Boxplot representing the GFP signal quantification after confocal microscopy imaging of transgenic GFP-NAC53/78 roots exposed to BTZ 10µM or CB-5083 10µM. Black dots represent one cell. Statistical difference is assessed by a Wilcoxon-Mann-Whitney test.

Figure 4. The transcriptional landscape of proteotoxic stress

(A) Log2FC mRNA levels of *NAC53* and *NAC78* transcripts after *Pst* infection of adult Col-0 plant leaves. The heatmap represent the mean of 4 biological replicates.

(B) Log2FC mRNA levels of 26S proteasome transcripts after *Pst* infection of Col-0 or *nac53-1 78-1* adult plant leaves. The heatmap represent the mean of 4 biological replicates. The experiment has been repeated 3 times with consistent results.

(C) Immunoblot against multiple 26S proteasome subunits on crude extracts of Col-0 or *nac53-1 78-1* adult plant leaves inoculated with *Pst* or mock solutions for 24h. Ponceau staining is used as loading control.

(D) Relative Log2FC abundance of representative 26S proteasome subunits in Col-0 or *nac53-1 78-1* adult plant leaves. The abundance is calculated relative to the mock conditions. Statistical differences are assessed via a Welch t.test (p values: n.s > 0.05, * < 0.05, ** < 0.01).

(E) Immunoblot against GFP on crude extract of *N. benthamiana* leaves transiently expressing GFP-NAC53/78 after mock treatment or *PstΔHopQ* infection for 8h. Ponceau staining is used as loading control.

(F) Immunoblot against GFP on extract of adult *A. thaliana* transgenics GFP-NAC53/78 subjected to mock treatment or *Pst* infection 8h by vacuum infiltration followed by IP with anti-GFP beads.

(G) Number of differentially expressed genes (DEGs) in the different conditions of the *nac53-1 78-1 Pst* RNAseq analysis. Total number of DEGs per condition is indicated. Colors indicate the proportion of DEGs up-regulated and down-regulated. DEGs are considered when |Log2FC| > 1.5. Genot. mock: *nac53-1 78-1* mock vs. Col-0 mock; WT *Pst*: Col-0 *Pst* vs. Col-0 mock; Mut. *Pst*: *nac53-1 78-1 Pst* vs. *nac53-1 78-1* mock; Genot. *Pst*: *nac53-1 78-1 Pst* vs. Col-0 *Pst*.

(H) Level of differential expression (Log2FC) of the 945 DEGs found in Genot. *Pst* (see panel G) for the several conditions analyzed.

(I) Cladogram of top 40 GO terms for BP enriched in the list of 945 DEGs. Colors represent broad GO clusters.

(J) Venn diagram representing the overlap between the 945 DEGs and DEGs from *rpt2a-2 Pma* (|Log2FC| > 0.5) or Col-0 MG132 24h (|Log2FC| > 0.5).

(K) Cladogram of top 30 GO terms for BP enriched in the list of 538 DEGs extracted from the combined analysis (panel J). For conciseness terms are hidden and grouped in 4 processes.

(L) Protein network of the genes from the 945 DEGs list related to the GO BP terms from panel K. Node colors refers to the 4 GO clusters from panel K.

Figure S4. Transcriptional analysis of proteotoxic stress reveals a trade-off between 26S proteasome and other biological process. Related to Figure 4

(A) mRNA level Log2FC of all 26S proteasome genes and associated interactors/chaperones in several conditions of the *nac53-1 78-1 Pst* RNAseq.

(B) Number of differentially expressed genes (DEGs) in the different conditions of the *nac53-1 78-1 Pst* RNAseq analysis. Total number of DEGs per condition is indicated. Colors indicate the proportion of DEGs up-regulated and down-regulated. DEGs are considered when |Log2FC| > 1.5. Genot. mock: *rpt2a-2* mock vs. Col-0 mock; WT *Pma*: Col-0 *Pma* vs. Col-0 mock; Mut. *Pma*: *rpt2a-2 Pma* vs. *nac53-1 78-1* mock; Genot. *Pma*: *rpt2a-2 Pma* vs. Col-0 *Pma*.

(C) mRNA levels Log2FC of the 981 DEGs found in Genot. *Pma* (see panel D) for the several conditions analyzed.

(D) mRNA level Log2FC of all 26S proteasome genes and associated interactors/chaperones in the several conditions of the *rpt2a-2 Pma* RNAseq.

(E) Cladogram of top 40 GO terms for BP enriched in the list of 945 DEGs. Colors represent the broad GO clusters.

(F) mRNA level Log2FC of the genes present in the 4 network modules from Figure 4L in the 3 Transcriptome used.

Figure 5. NAC53 and NAC78 coordinate the regulation of proteasome and photosynthesis gene expression through the same cis-element.

(A) Top 3 motifs found by STREME software in the promoter regions from the 4 network clusters (Figure 4L). PRCE-like elements from proteasome and PhANGs clusters are highlighted.

(B) 25bp region comprising the PRCE-like elements from LHCa3 and PSAD1 promoters used in this figure. The region corresponds to the probe sequence used in panel C and D. The PRCE is highlighted in red.

(C) Electro-Mobility Shift Assay (EMSA) of MBP-NAC53/78 with LHCa3/PSAD1 probes (see panel B). As a negative control, probes were incubated without MBP-NAC53/78 (-) or with MBP-NAC53/78 deleted for their DNA recognition motif (ΔRM). Experiment was repeated twice with similar results.

(D) EMSA competition assay of MBP-NAC53/78 association with LHCa3/PSAD1 probes. Competitor is applied at a concentration gradient (25X, 50X, 75X and 100X) indicated by the shade of grey. WT and mutated competitors are labelled TGGGC and AAAAA, respectively. Experiment was repeated twice with similar results.

(E) Boxplot representing association of GFP-NAC53/78 with LHCa3/PSAD1 PRCE in adult *A. thaliana* transgenics lines infected with *Pst* or mock for 8h after Chromatin Immunoprecipitation. The association is quantified as % of input and amplification of a region in the CDS is used as negative control.

(F) Immunoblot against mature PhANGs proteins in Col-0 or *nac53-1 78-1* adult plant leaves inoculated with *Pst* or mock solutions for 24h. Ponceau staining is used as loading control.

(G) Relative Log2FC abundance of PhANGs mature proteins immunoblotted in panel F. The abundance is calculated relative to the mock conditions. Statistical differences are assessed via a Welch t.test (p values: n.s > 0.05, * < 0.05, ** < 0.01).

(H) Photosystem II (PSII) activity measurement on Col-0 or *nac53-1 78-1* adult plants inoculated with *Pst* or mock solutions for 24h. Letters indicate the statistical group assessed by pairwise Welch t.test (p value < 0.05). The experiment was repeated 3 times with consistent results.

(I) Representative pictures of measurements from panel I. Fv/Fm values are represented by false color as indicated by the color gradient legend.

(J) Total chlorophylls and carotenoids from Col-0 or *nac53-1 78-1* adult plant leaves inoculated with *Pst* or mock solutions for 24h. Letters indicate the statistical group assessed by pairwise Wilcoxon-Mann-Whitney test (p value < 0.05). The experiment was repeated 3 times with consistent results.

Figure S5. Characterization of the NAC53/78-PRCE module in PhANGs promoters. Related to Figure 5.

(A) mRNA level Log2FC of the PhANGs clusters from Figure 4L in the 3 transcriptomes used. Genes are separated based on their associated process in the photosynthetic pathway.

(B) Mapping of the PRCE-like motifs in PhANGs promoter regions from panel A. Promoter regions are organized according to the order of the genes from panel A. Purple marks represent the position of the motifs based on their distance from the transcription starting site (TSS). The two red arrows highlight LHCa3 and PSAD1 promoter regions.

(C) Histograms representing the number of occurrences of the PRCE-like motifs across the 4 genes cluster from the network Figure 4L. Each bar represents a 20bp region, frequency *f* of promoters bearing at least one motif is indicated as a percentage.

(D) LHCa3/PSAD1 promoter activity measured by luminescence in Col-0 or *nac53-1 78-1* protoplasts extract transiently co-expressing LHCa3/PSAD1 reporter constructs and NAC53/78ΔTM. Log2FC is calculated from the luminescence level of protoplasts expressing

1479 the reporter construct alone. Replicates are a pool of at least two independent experiments.
1480 Letters indicate the statistical group assessed by pairwise Wilcoxon-Mann-Whitney test (p
1481 value < 0.05).
1482 (E) Promoter activity as calculated in panel D for LHCa3/PSAD1 promoters deleted for their
1483 respective DNA regions from Figure 5B. Replicates are a pool of at least two independent
1484 experiments. Letters indicate the statistical group assessed by pairwise Wilcoxon-Mann-
1485 Whitney test (p value < 0.05).
1486 (F-G) Boxplot representing the Log2FC mRNA level the indicated transcripts in Col-0, GFP-
1487 NAC53 or GFP-NAC78 seedlings treated with BTZ 10µM or mock solutions for 6h. Log2FC
1488 is calculated from Col-0 mock. Letters indicate the statistical group assessed by pairwise
1489 Wilcoxon-Mann-Whitney test (p value < 0.05).
1490 (H) Fresh weight of seedlings from indicated genotypes grown under the indicated treatments
1491 at 10 days after germination. Letters indicate the statistical group assessed by pairwise
1492 Wilcoxon-Mann-Whitney test (p value < 0.05). Experiment was repeated 3 times with
1493 consistent results.
1494 (I) Representative phenotypic pictures related to panel D.
1495 **Figure 6. The proteasome autoregulatory feedback loop monitors photosynthesis**
1496 **homeostasis during stress responses**
1497 (A) Photosynthetic pigment content from Col-0 or *nac53-1 78-1* adult plant leaves infiltrated
1498 with Lin 200µM, BTZ 2µM or mock solutions for 24h. Content is expressed in percentage
1499 relative to Col-0 mock. Letters indicate the statistical group assessed by pairwise Wilcoxon-
1500 Mann-Whitney test (p value < 0.05). The experiment was repeated 3 times with consistent
1501 results.
1502 (B) Log2FC mRNA level of the indicated transcripts in Col-0, *nac53-1 78-1* adult plants leaves
1503 Lin 200µM, BTZ 2µM or mock solutions for 24h. Log2FC is calculated from Col-0 mock and
1504 *PDH1* is used as negative control. Statistical differences are assessed with a Welch t-test (p
1505 values: n.s. > 0.05, * < 0.05, ** < 0.01). The experiment was repeated twice with consistent
1506 results.
1507 (C) Fresh weight of seedlings grown under the indicated treatments at 10-14 day after
1508 germination. The fresh weight is represented as a percentage of Col-0 mock conditions. Letters
1509 indicate the statistical groups assessed by pairwise Wilcoxon-Mann-Whitney test (p value <
1510 0.05). Every treatment has been repeated at least twice with consistent results. Representative
1511 phenotypic pictures are included.
1512 (D) Bacterial density shown as Log10 Colony-Forming-Unit (CFU) per leaf cm^2 in Col-0 and
1513 *hrd1a hrd1b* plants. Statistical significance is assessed by a Welch t-test (p values: * < 0.05).
1514 The experiment has been repeated three times with consistent results.
1515 (E) Correlation heatmap of the 54 26S proteasome subunit genes and the expression of 68
1516 PhANGs from publicly available 1223 RNAseq libraries identified in this study.
1517 **Figure S6. The proteasome autoregulatory feedback loop transcriptional signature is a**
1518 **systemic response to environmental cues. Related to Figure 6.**
1519 (A) PSII activity measurement on Col-0 and *nac53-1 78-1* treated as indicated in Figure 6A.
1520 Replicates are a pool of 3 independent experiments. Letters indicate the statistical group
1521 assessed by pairwise Wilcoxon-Mann-Whitney test (p value < 0.05).
1522 (B) PSII activity measurement on Col-0 and *hrd1a hrd1b* adult plant leaves inoculated with *Pst*
1523 or mock solutions for 24h. Letters indicate the statistical group assessed by pairwise Welch
1524 t.test (p value < 0.05). The experiment was repeated 2 times with consistent results.
1525 (C) Confocal microscopy pictures of transgenic GFP-NAC53/78 *A. thaliana* roots exposed to
1526 mock treatment, MV 100µM, GDA 100µM and Lin 100µM for 2h. The treatments were
1527 repeated at least three times with similar observations. Scale bars = 10µm
1528 (D) Density functions of the 54 26S proteasome genes and 68 PhANGs transcripts (Log2FC)
1529 in the different transcriptome projects. Log2FC limits are -10 to +10. Treatment types and

relevant condition information are provided in the figure. Plots are separated by treatment groups and subdivided by experiments.

Figure 7. ER-anchored protein sorting (ERAPS) controls the fate of two proteasome activators for intracellular organelle communication during proteotoxic stress.

In steady state conditions, the ER-anchored protein sorting system (ERAPS) promotes the constitutive degradation of NAC53/78 via the 26S proteasome. Meanwhile, PhANGs expression is activated and subsequent chloroplastic import permits the maintenance of active photosynthesis. Upon proteotoxic stress, the chloroplast import machinery is targeted for proteasomal degradation. This leads to an accumulation of PhANGs precursors which are therefore subjected to proteasomal degradation, inducing proteotoxicity. Thus, to avoid proteotoxicity, the ERAPS system facilitates the nuclear translocation of NAC53/78, to activate the production of a new proteasome complex and to repress PhANGs expression to mitigate substrate accumulation.

REFERENCES

Albert, S., Wietrzynski, W., Lee, C.W., Schaffer, M., Beck, F., Schuller, J.M., Salome, P.A., Plitzko, J.M., Baumeister, W., and Engel, B.D. (2020). Direct visualization of degradation microcompartments at the ER membrane. Proc Natl Acad Sci U S A *117*, 1069-1080.

Baird, L., Tsujita, T., Kobayashi, E.H., Funayama, R., Nagashima, T., Nakayama, K., and Yamamoto, M. (2017). A Homeostatic Shift Facilitates Endoplasmic Reticulum Proteostasis through Transcriptional Integration of Proteostatic Stress Response Pathways. Mol Cell Biol *37*.

Binder, A., Lambert, J., Morbitzer, R., Popp, C., Ott, T., Lahaye, T., and Parniske, M. (2014). A modular plasmid assembly kit for multigene expression, gene silencing and silencing rescue in plants. PLoS One *9*, e88218.

Boos, F., Kramer, L., Groh, C., Jung, F., Haberkant, P., Stein, F., Wollweber, F., Gackstatter, A., Zoller, E., van der Laan, M.*, et al.* (2019). Mitochondrial protein-induced stress triggers a global adaptive transcriptional programme. Nat Cell Biol *21*, 442-451.

Bragoszewski, P., Turek, M., and Chacinska, A. (2017). Control of mitochondrial biogenesis and function by the ubiquitin-proteasome system. Open Biol *7*.

Chen, Q., Zhong, Y., Wu, Y., Liu, L., Wang, P., Liu, R., Cui, F., Li, Q., Yang, X., Fang, S.*, et al.* (2016). HRD1-mediated ERAD tuning of ER-bound E2 is conserved between plants and mammals. Nat Plants *2*, 16094.

Christianson, J.C., and Ye, Y. (2014). Cleaning up in the endoplasmic reticulum: ubiquitin in charge. Nat Struct Mol Biol *21*, 325-335.

Clough, S.J., and Bent, A.F. (1998). Floral dip: a simplified method for Agrobacterium-mediated transformation of Arabidopsis thaliana. Plant J *16*, 735-743.

Colberg, L., Cammann, C., Greinacher, A., and Seifert, U. (2020). Structure and function of the ubiquitin-proteasome system in platelets. J Thromb Haemost *18*, 771-780.

Diaz-Tielas, C., Grana, E., Sanchez-Moreiras, A.M., Reigosa, M.J., Vaughn, J.N., Pan, Z., Bajsa-Hirschel, J., Duke, M.V., and Duke, S.O. (2019). Transcriptome responses to the natural phytotoxin t-chalcone in Arabidopsis thaliana L. Pest Manag Sci *75*, 2490-2504.

Duval, M., Hsieh, T.-F., Kim, S.Y., and Thomas, T.L. (2002). Molecular characterization of AtNAM: a member of theArabidopsis NAC domain superfamily. Plant Molecular Biology *50*, 237-248.

Farmer, L.M., Book, A.J., Lee, K.H., Lin, Y.L., Fu, H., and Vierstra, R.D. (2010). The RAD23 family provides an essential connection between the 26S proteasome and ubiquitylated proteins in Arabidopsis. Plant Cell *22*, 124-142.

Fonseca, D., and Carvalho, P. (2019). EGAD! There is an ERAD doppelganger in the Golgi. EMBO J *38*, e102679.

Gallo-Oller, G., Ordoñez, R., and Dotor, J. (2018). A new background subtraction method for Western blot densitometry band quantification through image analysis software. Journal of Immunological Methods *457*, 1-5.
Ge, S.X., Jung, D., and Yao, R. (2020). ShinyGO: a graphical gene-set enrichment tool for animals and plants. Bioinformatics *36*, 2628-2629.
Gladman, N.P., Marshall, R.S., Lee, K.H., and Vierstra, R.D. (2016). The Proteasome Stress Regulon Is Controlled by a Pair of NAC Transcription Factors in Arabidopsis. Plant Cell *28*, 1279-1296.
Grimmer, J., Helm, S., Dobritzsch, D., Hause, G., Shema, G., Zahedi, R.P., and Baginsky, S. (2020). Mild proteasomal stress improves photosynthetic performance in Arabidopsis chloroplasts. Nat Commun *11*, 1662.
Gureev, A.P., Shaforostova, E.A., and Popov, V.N. (2019). Regulation of Mitochondrial Biogenesis as a Way for Active Longevity: Interaction Between the Nrf2 and PGC-1alpha Signaling Pathways. Front Genet *10*, 435.
Hao, Y.J., Song, Q.X., Chen, H.W., Zou, H.F., Wei, W., Kang, X.S., Ma, B., Zhang, W.K., Zhang, J.S., and Chen, S.Y. (2010). Plant NAC-type transcription factor proteins contain a NARD domain for repression of transcriptional activation. Planta *232*, 1033-1043.
Hristou, A., Grimmer, J., and Baginsky, S. (2020). The Secret Life of Chloroplast Precursor Proteins in the Cytosol. Mol Plant *13*, 1111-1113.
Hu, X., Zou, R., Zhang, Z., Ji, J., Li, J., Huo, X.-Y., Liu, D., Ge, M.-X., Cui, M.-K., Wu, M.-Z.*, et al.* (2023). UBE4A catalyzes NRF1 ubiquitination and facilitates DDI2-mediated NRF1 cleavage. Biochimica et Biophysica Acta (BBA) - Gene Regulatory Mechanisms *1866*, 194937.
Jayaraj, G.G., Hipp, M.S., and Hartl, F.U. (2020). Functional Modules of the Proteostasis Network. Cold Spring Harb Perspect Biol *12*.
Kacprzak, S.M., Mochizuki, N., Naranjo, B., Xu, D., Leister, D., Kleine, T., Okamoto, H., and Terry, M.J. (2019). Plastid-to-Nucleus Retrograde Signalling during Chloroplast Biogenesis Does Not Require ABI4. Plant Physiol *179*, 18-23.
Kliza, K., Taumer, C., Pinzuti, I., Franz-Wachtel, M., Kunzelmann, S., Stieglitz, B., Macek, B., and Husnjak, K. (2017). Internally tagged ubiquitin: a tool to identify linear polyubiquitin-modified proteins by mass spectrometry. Nature Methods *14*, 504-512.
Kourelis, J., Kaschani, F., Grosse-Holz, F.M., Homma, F., Kaiser, M., and van der Hoorn, R.A.L. (2019). A homology-guided, genome-based proteome for improved proteomics in the alloploid Nicotiana benthamiana. BMC Genomics *20*, 722.
Koussevitzky, S., Nott, A., Mockler, T.C., Hong, F., Sachetto-Martins, G., Surpin, M., Lim, J., Mittler, R., and Chory, J. (2007). Signals from Chloroplasts Converge to Regulate Nuclear Gene Expression. Science *316*, 715-719.
Kramer, L., Groh, C., and Herrmann, J.M. (2021). The proteasome: friend and foe of mitochondrial biogenesis. FEBS Lett *595*, 1223-1238.
Kuhn, L., Vincent, T., Hammann, P., and Zuber, H. (2023). Exploring Protein Interactome Data with IPinquiry: Statistical Analysis and Data Visualization by Spectral Counts. In Statistical Analysis of Proteomic Data: Methods and Tools, T. Burger, ed. (New York, NY: Springer US), pp. 243-265.
Langin, G., Gonzalez-Fuente, M., and Üstün, S. (2023). The Plant Ubiquitin-Proteasome System as a Target for Microbial Manipulation. Annu Rev Phytopathol *61*, 351-375.
Langin, G., Gouguet, P., and Üstün, S. (2020). Microbial Effector Proteins - A Journey through the Proteolytic Landscape. Trends Microbiol *28*, 523-535.
Langin, G., and Üstün, S. (2023). A Pipeline to Monitor Proteasome Homeostasis in Plants. In Plant Proteostasis: Methods and Protocols, L.M. Lois, and M. Trujillo, eds. (New York, NY: Springer US), pp. 351-363.
Lee, K.H., Minami, A., Marshall, R.S., Book, A.J., Farmer, L.M., Walker, J.M., and Vierstra, R.D. (2011). The RPT2 subunit of the 26S proteasome directs complex assembly, histone

1631 dynamics, and gametophyte and sporophyte development in Arabidopsis. Plant Cell *23*, 4298-
1632 4317.
1633 Leister, D.S., A. (2003). From Genes to Photosynthesis in Arabidopsis thaliana. Int Rev Cytol
1634 *228*.
1635 Leong, J.X., Raffeiner, M., Spinti, D., Langin, G., Franz-Wachtel, M., Guzman, A.R., Kim,
1636 J.G., Pandey, P., Minina, A.E., Macek, B.*, et al.* (2022). A bacterial effector counteracts host
1637 autophagy by promoting degradation of an autophagy component. Embo J *41*, e110352.
1638 Li, J., Yuan, J., Li, Y., Sun, H., Ma, T., Huai, J., Yang, W., Zhang, W., and Lin, R. (2022). The
1639 CDC48 complex mediates ubiquitin-dependent degradation of intra-chloroplast proteins in
1640 plants. Cell Rep *39*, 110664.
1641 Liao, P.C., Wolken, D.M.A., Serrano, E., Srivastava, P., and Pon, L.A. (2020). Mitochondria-
1642 Associated Degradation Pathway (MAD) Function beyond the Outer Membrane. Cell Rep *32*,
1643 107902.
1644 Lichtenthaler, H.K. (1987). [34] Chlorophylls and carotenoids: Pigments of photosynthetic
1645 biomembranes. In Methods in Enzymology (Academic Press), pp. 350-382.
1646 Ling, Q., Broad, W., Trosch, R., Topel, M., Demiral Sert, T., Lymperopoulos, P., Baldwin, A.,
1647 and Jarvis, R.P. (2019). Ubiquitin-dependent chloroplast-associated protein degradation in
1648 plants. Science *363*.
1649 Littlejohn, G.R., Breen, S., Smirnoff, N., and Grant, M. (2021). Chloroplast immunity
1650 illuminated. New Phytol *229*, 3088-3107.
1651 Love, M.I., Huber, W., and Anders, S. (2014). Moderated estimation of fold change and
1652 dispersion for RNA-seq data with DESeq2. Genome Biology *15*, 550.
1653 Ma, M., and Liu, Z.L. (2010). Comparative transcriptome profiling analyses during the lag
1654 phase uncover YAP1, PDR1, PDR3, RPN4, and HSF1 as key regulatory genes in genomic
1655 adaptation to the lignocellulose derived inhibitor HMF for Saccharomyces cerevisiae. BMC
1656 Genomics *11*, 660.
1657 Maekawa, T., Kusakabe, M., Shimoda, Y., Sato, S., Tabata, S., Murooka, Y., and Hayashi, M.
1658 (2008). Polyubiquitin Promoter-Based Binary Vectors for Overexpression and Gene Silencing
1659 in Lotus japonicus. Molecular Plant-Microbe Interactions *21*, 375-382.
1660 Mannhaupt, G., Schnall, R., Karpov, V., Vetter, I., and Feldmann, H. (1999). Rpn4p acts as a
1661 transcription factor by binding to PACE, a nonamer box found upstream of 26S proteasomal
1662 and other genes in yeast. FEBS Letters *450*, 27-34.
1663 Marshall, R.S., Hua, Z., Mali, S., McLoughlin, F., and Vierstra, R.D. (2019). ATG8-Binding
1664 UIM Proteins Define a New Class of Autophagy Adaptors and Receptors. Cell *177*, 766-781
1665 e724.
1666 Marshall, R.S., and Vierstra, R.D. (2019). Dynamic Regulation of the 26S Proteasome: From
1667 Synthesis to Degradation. Front Mol Biosci *6*, 40.
1668 Ng, S., Ivanova, A., Duncan, O., Law, S.R., Van Aken, O., De Clercq, I., Wang, Y., Carrie, C.,
1669 Xu, L., Kmiec, B.*, et al.* (2013). A membrane-bound NAC transcription factor, ANAC017,
1670 mediates mitochondrial retrograde signaling in Arabidopsis. Plant Cell *25*, 3450-3471.
1671 Nguyen, H.M., Schippers, J.H., Goni-Ramos, O., Christoph, M.P., Dortay, H., van der Hoorn,
1672 R.A., and Mueller-Roeber, B. (2013). An upstream regulator of the 26S proteasome modulates
1673 organ size in Arabidopsis thaliana. Plant J *74*, 25-36.
1674 Orosa, B., Üstün, S., Calderon Villalobos, L.I.A., Genschik, P., Gibbs, D., Holdsworth, M.J.,
1675 Isono, E., Lois, M., Trujillo, M., and Sadanandom, A. (2020). Plant proteostasis - shaping the
1676 proteome: a research community aiming to understand molecular mechanisms that control
1677 protein abundance. New Phytol *227*, 1028-1033.
1678 Page, M.T., Kacprzak, S.M., Mochizuki, N., Okamoto, H., Smith, A.G., and Terry, M.J. (2017).
1679 Seedlings Lacking the PTM Protein Do Not Show a genomes uncoupled (gun) Mutant
1680 Phenotype. Plant Physiol *174*, 21-26.

Pastor-Cantizano, N., Ko, D.K., Angelos, E., Pu, Y., and Brandizzi, F. (2020). Functional Diversification of ER Stress Responses in Arabidopsis. Trends Biochem Sci *45*, 123-136.
Peters, L.Z., Hazan, R., Breker, M., Schuldiner, M., and Ben-Aroya, S. (2013). Formation and dissociation of proteasome storage granules are regulated by cytosolic pH. J Cell Biol *201*, 663-671.
Radhakrishnan, S.K., den Besten, W., and Deshaies, R.J. (2014). p97-dependent retrotranslocation and proteolytic processing govern formation of active Nrf1 upon proteasome inhibition. Elife *3*, e01856.
Raffeiner, M., Zhu, S., Gonzalez-Fuente, M., and Üstün, S. (2023). Interplay between autophagy and proteasome during protein turnover. Trends Plant Sci *28*, 698-714.
Richter, A.S., Nagele, T., Grimm, B., Kaufmann, K., Schroda, M., Leister, D., and Kleine, T. (2023). Retrograde signaling in plants: A critical review focusing on the GUN pathway and beyond. Plant Commun *4*, 100511.
Ruvkun, G., and Lehrbach, N. (2023). Regulation and Functions of the ER-Associated Nrf1 Transcription Factor. Cold Spring Harb Perspect Biol *15*.
Sampaio-Marques, B., and Ludovico, P. (2018). Linking cellular proteostasis to yeast longevity. FEMS Yeast Res *18*.
Schreiber, U. (2004). Pulse-Amplitude-Modulation (PAM) Fluorometry and Saturation Pulse Method: An Overview. In Chlorophyll a Fluorescence: A Signature of Photosynthesis, G.C. Papageorgiou, and Govindjee, eds. (Dordrecht: Springer Netherlands), pp. 279-319.
Schwanhäusser, B., Busse, D., Li, N., Dittmar, G., Schuchhardt, J., Wolf, J., Chen, W., and Selbach, M. (2011). Global quantification of mammalian gene expression control. Nature *473*, 337-342.
Seo, P.J., Kim, S.G., and Park, C.M. (2008). Membrane-bound transcription factors in plants. Trends Plant Sci *13*, 550-556.
Sha, Z., and Goldberg, A.L. (2014). Proteasome-mediated processing of Nrf1 is essential for coordinate induction of all proteasome subunits and p97. Curr Biol *24*, 1573-1583.
Shih, C.F., Hsu, W.H., Peng, Y.J., and Yang, C.H. (2014). The NAC-like gene ANTHER INDEHISCENCE FACTOR acts as a repressor that controls anther dehiscence by regulating genes in the jasmonate biosynthesis pathway in Arabidopsis. J Exp Bot *65*, 621-639.
Shirozu, R., Yashiroda, H., and Murata, S. (2015). Identification of minimum Rpn4-responsive elements in genes related to proteasome functions. FEBS Lett *589*, 933-940.
Shpilka, T., Du, Y., Yang, Q., Melber, A., Uma Naresh, N., Lavelle, J., Kim, S., Liu, P., Weidberg, H., Li, R.*, et al.* (2021). UPR(mt) scales mitochondrial network expansion with protein synthesis via mitochondrial import in Caenorhabditis elegans. Nat Commun *12*, 479.
Steffen, J., Seeger, M., Koch, A., and Kruger, E. (2010). Proteasomal degradation is transcriptionally controlled by TCF11 via an ERAD-dependent feedback loop. Mol Cell *40*, 147-158.
Su, W., Liu, Y., Xia, Y., Hong, Z., and Li, J. (2011). Conserved endoplasmic reticulum-associated degradation system to eliminate mutated receptor-like kinases in Arabidopsis. Proceedings of the National Academy of Sciences *108*, 870-875.
Sun, X., Feng, P., Xu, X., Guo, H., Ma, J., Chi, W., Lin, R., Lu, C., and Zhang, L. (2011). A chloroplast envelope-bound PHD transcription factor mediates chloroplast signals to the nucleus. Nat Commun *2*, 477.
Tanaka, K., Mizushima, T., and Saeki, Y. (2012). The proteasome: molecular machinery and pathophysiological roles. Biol Chem *393*, 217-234.
Tokumaru, M., Adachi, F., Toda, M., Ito-Inaba, Y., Yazu, F., Hirosawa, Y., Sakakibara, Y., Suiko, M., Kakizaki, T., and Inaba, T. (2017). Ubiquitin-Proteasome Dependent Regulation of the GOLDEN2-LIKE 1 Transcription Factor in Response to Plastid Signals. Plant Physiol *173*, 524-535.

Ulasov, A.V., Rosenkranz, A.A., Georgiev, G.P., and Sobolev, A.S. (2022). Nrf2/Keap1/ARE signaling: Towards specific regulation. Life Sci *291*, 120111.

Üstün, S., Hafrén, A., Liu, Q., Marshall, R.S., Minina, E.A., Bozhkov, P.V., Vierstra, R.D., and Hofius, D. (2018). Bacteria Exploit Autophagy for Proteasome Degradation and Enhanced Virulence in Plants. Plant Cell *30*, 668-685.

Üstün, S., Sheikh, A., Gimenez-Ibanez, S., Jones, A., Ntoukakis, V., and Börnke, F. (2016). The Proteasome Acts as a Hub for Plant Immunity and Is Targeted by Pseudomonas Type III Effectors. Plant Physiol *172*, 1941-1958.

Wang, X., Xu, H., Ju, D., and Xie, Y. (2008). Disruption of Rpn4-induced proteasome expression in Saccharomyces cerevisiae reduces cell viability under stressed conditions. Genetics *180*, 1945-1953.

Wang, X., Yen, J., Kaiser, P., and Huang, L. (2010). Regulation of the 26S proteasome complex during oxidative stress. Sci Signal *3*, ra88.

Waters, M.T., Wang, P., Korkaric, M., Capper, R.G., Saunders, N.J., and Langdale, J.A. (2009). GLK transcription factors coordinate expression of the photosynthetic apparatus in Arabidopsis. Plant Cell *21*, 1109-1128.

Weidberg, H., and Amon, A. (2018). MitoCPR-A surveillance pathway that protects mitochondria in response to protein import stress. Science *360*.

Welner, D.H., Deeba, F., Lo Leggio, L., and Skriver, K. (2016). NAC Transcription Factors: From Structure to Function in Stress-Associated Networks. In Plant Transcription Factors, pp. 199-212.

Woodson, J.D., and Chory, J. (2012). Organelle signaling: how stressed chloroplasts communicate with the nucleus. Curr Biol *22*, R690-692.

Wu, G.Z., Meyer, E.H., Richter, A.S., Schuster, M., Ling, Q., Schottler, M.A., Walther, D., Zoschke, R., Grimm, B., Jarvis, R.P.*, et al.* (2019). Control of retrograde signalling by protein import and cytosolic folding stress. Nat Plants *5*, 525-538.

Xie, Y., and Varshavsky, A. (2001). RPN4 is a ligand, substrate, and transcriptional regulator of the 26S proteasome: A negative feedback circuit. Proceedings of the National Academy of Sciences *98*, 3056-3061.

Xie, Y.V., A. (2001). RPN4 is a ligand, substrate, and transcriptional regulator of the 26S proteasome: A negative feedback circuit. Proc Natl Acad Sci U S A *98*, 3056-3061.

Yagishita, N., Aratani, S., Leach, C., Amano, T., Yamano, Y., Nakatani, K., Nishioka, K., and Nakajima, T. (2012). RING-finger type E3 ubiquitin ligase inhibitors as novel candidates for the treatment of rheumatoid arthritis. Int J Mol Med *30*, 1281-1286.

Yoo, S.D., Cho, Y.H., and Sheen, J. (2007). Arabidopsis mesophyll protoplasts: a versatile cell system for transient gene expression analysis. Nat Protoc *2*, 1565-1572.

Zhang, H., Zhang, F., Yu, Y., Feng, L., Jia, J., Liu, B., Li, B., Guo, H., and Zhai, J. (2020). A Comprehensive Online Database for Exploring approximately 20,000 Public Arabidopsis RNA-Seq Libraries. Mol Plant *13*, 1231-1233.

Zhou, H.J., Wang, J., Yao, B., Wong, S., Djakovic, S., Kumar, B., Rice, J., Valle, E., Soriano, F., Menon, M.K.*, et al.* (2015). Discovery of a First-in-Class, Potent, Selective, and Orally Bioavailable Inhibitor of the p97 AAA ATPase (CB-5083). J Med Chem *58*, 9480-9497.